

# Understanding the geodetic signature of large aquifer systems: Example of the Ozark Plateaus in Central United States

Stacy Larochelle<sup>1</sup>, Kristel Chanard<sup>2,3</sup>, Luce Fleitout<sup>4</sup>, Jrome Fortin<sup>5</sup>, Adriano Gualandi<sup>1,6</sup>, Laurent Longuevergne<sup>7</sup>, Paul Rebischung<sup>2,3</sup>, Sophie Violette<sup>4,8</sup>, and Jean-Philippe Avouac<sup>1</sup>

<sup>1</sup>Geological and Planetary Sciences, California Institute of Technology, Pasadena, California, USA

<sup>2</sup>Universit de Paris, Institut de physique du globe de Paris, CNRS, IGN, Paris, France

<sup>3</sup>ENSG-Gomatique, IGN, Marne-la-Valle, France

<sup>4</sup>Laboratoire de Gologie, cole Normale Suprieure, Universit PSL, CNRS, Paris, France

<sup>5</sup>University PSL, CNRS UMR 8538, Paris, France

<sup>6</sup>Istituto Nazionale di Geofisica e Vulcanologia, Osservatorio Nazionale Terremoti, Rome, Italy

<sup>7</sup>Univ Rennes, CNRS, Geosciences Rennes - UMR 6118, F-35000 Rennes, France

<sup>8</sup>Sorbonne University, UFR.918, Paris, France

## Key Points:

- We characterize seasonal and multiannual groundwater fluctuations with an Independent Component Analysis.
- We separate and model the hydrological loading and poroelastic deformation fields captured by GNSS.
- We infer relatively low elastic moduli from the extracted poroelastic displacements and groundwater fluctuations.

---

Corresponding author: Stacy Larochelle, [stacy.larochelle@caltech.edu](mailto:stacy.larochelle@caltech.edu)

This article has been accepted for publication and undergone full peer review but has not been through the copyediting, typesetting, pagination and proofreading process, which may lead to differences between this version and the [Version of Record](#). Please cite this article as [doi: 10.1029/2021JB023097](https://doi.org/10.1029/2021JB023097).

This article is protected by copyright. All rights reserved.

## Abstract

The continuous redistribution of water involved in the hydrologic cycle leads to deformation of the solid Earth. On a global scale, this deformation is well explained by the loading imposed by hydrological mass variations and can be quantified to first order with space-based gravimetric and geodetic measurements. At the regional scale, however, aquifer systems also undergo poroelastic deformation in response to groundwater fluctuations. Disentangling these related but distinct 3D deformation fields from geodetic time series is essential to accurately invert for changes in continental water mass, to understand the mechanical response of aquifers to internal pressure changes as well as to correct time series for these known effects. Here, we demonstrate a methodology to accomplish this task by considering the example of the well-instrumented Ozark Plateaus Aquifer System (OPAS) in central United States. We begin by characterizing the most important sources of groundwater level variations in the spatially heterogeneous piezometer dataset using an Independent Component Analysis. Then, to estimate the associated poroelastic displacements, we project geodetic time series corrected for hydrological loading effects onto the dominant groundwater temporal functions. We interpret the extracted displacements in light of analytical solutions and a 2D model relating groundwater level variations to surface displacements. In particular, the relatively low estimates of elastic moduli inferred from the poroelastic displacements and groundwater fluctuations may be indicative of aquifer layers with a high fracture density. Our findings suggest that OPAS undergoes significant poroelastic deformation, including highly heterogeneous horizontal poroelastic displacements.

## Plain Language Summary

A number of hydrological processes can deform the solid Earth. Measuring this deformation through space-based geodesy offers an opportunity to study these hydrologic processes and infer properties of the sub-surface. In the case of an aquifer, surface displacements can arise from changes in total water mass, which load the Earth, as well as from changes in groundwater pressure which alter stresses in the aquifer and in the surrounding medium. In this study, we describe a methodology to extract and separate these distinct but related deformation signals from GNSS time series and hence infer mechanical properties of the aquifer system by using satellite gravimetry data, local groundwater level measurements as well as a blind source separation technique. We also present a mathematical framework to study surface displacements resulting from variations in groundwater pressure in a medium with heterogeneous elastic properties. We demonstrate the methodology in the Ozark Plateaus Aquifer System in central United States.

## 1 Introduction

Hydrological processes occurring at the surface of the Earth redistribute continental water mass and the resulting load variations deform the solid Earth. The primarily seasonal deformation can be measured with space-based geodetic techniques such as GNSS (Global Navigation Satellite System) (Blewitt et al., 2001; van Dam et al., 2001; Dong et al., 2002). It is thus possible to infer fluctuations in continental water storage from GNSS time series (Ouellette et al., 2013; Argus et al., 2014, 2017; Borsa et al., 2014; Fu et al., 2015; Adusumilli et al., 2019; Ferreira et al., 2019) assuming that the regional deformation field induced by hydrology can be separated from other geodetic signals and/or systematic errors (Chanard et al., 2020). Such regional-scale constraints on hydrological fluctuations help bridge the gap between *in situ* measurements (e.g., groundwater monitoring wells, stream gauges) and continental-scale observations from the Gravity Recovery and Climate Experiment (GRACE) mission (Tapley et al., 2004).

71 At a global scale, seasonal signals in GNSS time series are not entirely explained  
72 by GRACE-measured hydrological loading (Chanard et al., 2018). Additional defor-  
73 mation mechanisms related to groundwater and temperature variations are thought  
74 to explain a significant fraction of this seasonal variance (Tsai, 2011). In particular,  
75 aquifer basins - which store roughly 30% of Earth's freshwater reserves (Shiklomanov,  
76 1993) - are prone to poroelastic swelling in addition to hydrological loading (Wang,  
77 2000). An increase in surface and groundwater mass (Figure 1A) translates to an  
78 increase of load which leads to subsidence and horizontal displacements towards the  
79 added load (Boussinesq, 1885; Verruijt, 2009) (Figure 1B). At the same time, the  
80 increase in groundwater storage rises pore pressure levels and generates eigenstrains  
81 within the aquifer and hence induces uplift and radially outward surface displacements  
82 (King et al., 2007; Galloway & Burbey, 2011) (Figure 1C).

83 Separating the contributions of hydrological loading and poroelasticity in geode-  
84 tic time series is crucial to better understand the physics of either deformation processes  
85 and quantify fluctuations in total water storage. Extracting the poroelastic defor-  
86 mation field has direct implications for inferring, at the field scale, the hydromechanical  
87 properties of aquifer systems which are tightly linked to hydrodynamical properties. In-  
88 deed, surface deformation provides information about internal aquifer processes which  
89 are generally not accessible otherwise. Such insight could improve the representation  
90 of groundwater within global and regional hydrological models and hence strengthen  
91 their predictive ability (Gleeson et al., 2021). Estimates of effective elastic moduli  
92 obtained through geodesy also provide measurements at a scale and loading rate (i.e.,  
93 quasi-static) relevant for geohydrologic processes and complementary to those obtained  
94 through seismology and laboratory experiments (Carlson et al., 2020). Beyond hydro-  
95 logical applications, characterizing the seasonal content of geodetic time series is also  
96 essential to isolate the deformation associated with tectonic processes (Michel et al.,  
97 2019; Vergnolle et al., 2010) and to investigate the response of seismicity to seasonal  
98 forcings (Bettinelli et al., 2008; Craig et al., 2017; C. W. Johnson et al., 2017).

99 A number of studies, mostly using Interferometric Synthetic Aperture Radar  
100 (InSAR), have demonstrated the feasibility of documenting aquifer dynamics and in-  
101 ferring their mechanical properties based on remote sensing measurements of surface  
102 deformation and *in situ* measurements of groundwater levels (Amelung et al., 1999;  
103 Bell et al., 2008; Wisely & Schmidt, 2010; Galloway & Burbey, 2011; Chaussard et  
104 al., 2014, 2017; Miller et al., 2017; Ojha et al., 2018; Riel et al., 2018; Alghamdi et al.,  
105 2020; Hu & Bürgmann, 2020; Gualandi & Liu, 2021). Most of these studies focused on  
106 aquifer basins where the poroelastic response dominates the local deformation field.  
107 At a regional scale, however, both deformation fields vary spatially and are not easily  
108 separated given the codependency of these deformation processes.

109 Here, we describe a new methodology to extract poroelastic deformation from  
110 GNSS time series by harnessing observations from the GRACE satellites and *in situ*  
111 groundwater monitoring wells as well as a blind source separation technique (Gua-  
112 landi et al., 2016). Focusing on GNSS data as opposed to InSAR provides (1) a  
113 complementary set of geodetic observations with different systematic errors, (2) the  
114 opportunity to study larger aquifer systems at which InSAR processing becomes chal-  
115 lenging and (3) a means to correct for known hydrological effects in GNSS time series  
116 extensively used in tectonic studies. Indeed, GNSS provides insight into the 3D surface  
117 deformation field complementary to InSAR, particularly when it comes to horizontal  
118 displacements. This is important because, as we emphasize in this work, horizontal  
119 and vertical deformation fields arising from different mechanisms can have distinct  
120 spatial signatures.

121 Previous studies have described poroelastic deformation fields using a number of  
122 modeling frameworks, including the USGS modular finite-difference groundwater flow  
123 model (MODFLOW) (Hoffmann & Wilson, 2003), finite strain cuboids in a homoge-

124 neous elastic half-space (Barbot et al., 2017; Silverii et al., 2019; Hu & Bürgmann,  
125 2020) and mixed finite element models (Ferronato et al., 2010; Alghamdi et al., 2020).  
126 In this work, we present an alternative framework to characterize the vertical and  
127 horizontal surface displacements arising from poroelastic eigenstrains in an unconfined  
128 aquifer with heterogeneous elastic properties (Fleitout & Chanard, 2018). We hope  
129 that the resulting (semi-)analytical solutions can serve as an intermediate between  
130 models with homogeneous elastic properties and more involved numerical models, and  
131 hence provide further insight into the complex, three-dimensional deformation field of  
132 aquifer systems.

133 The manuscript is organized as follows: We first introduce the geohydrological  
134 setting and data sets of our study area in Section 2. We selected the Ozark Plateaus  
135 Aquifer System (OPAS) in central United States to test the method because of the rel-  
136 atively quiescent tectonic setting (Craig & Calais, 2014; Calais et al., 2016), the data  
137 availability and the well-documented geohydrological setting (e.g., Imes & Emmett,  
138 1994; Hays et al., 2016; Westerman et al., 2016; Knierim et al., 2017). In Section 3, we  
139 characterize the heterogeneous groundwater level dataset with an Independent Com-  
140 ponent Analysis (ICA). We then present analytical solutions for simple disk loading  
141 and aquifer scenarios before extracting the 3D poroelastic deformation field from the  
142 GNSS time series in Section 4. We conclude the study by inferring the heterogeneous  
143 distribution of elastic moduli in OPAS from the extracted groundwater level variations  
144 and vertical poroelastic displacements in Section 5.

## 145 2 Regional setting and data sets

### 146 2.1 The Ozark Plateaus Aquifer System (OPAS)

147 OPAS is a large system of aquifers and confining units in the Mississippi River  
148 basin in central United States (Figure 2). The system is bounded by the Mississippi  
149 River and its alluvial plain, the Missouri River and Arkansas River to the east, north  
150 and south, respectively, and by a saline to freshwater transition zone to the west  
151 (Imes & Emmett, 1994) (Figure 2A). Although it is a significant source of water for  
152 agricultural and public supply in the region, groundwater use in OPAS represents a  
153 relatively small portion of the hydrologic budget – about 2% of aquifer recharge (Hays  
154 et al., 2016). Most groundwater recharge flows laterally, feeding other aquifers and  
155 sustaining streams, lakes and wetlands (Hays et al., 2016). Nonetheless, groundwater  
156 pumping does cause localized cones of depression around certain urban areas such as  
157 Springfield, Missouri (Imes, 1989).

158 OPAS is composed of interbedded layers of carbonate and clastic deposits around  
159 the topographic high Ozark dome (Hays et al., 2016; Westerman et al., 2016). The  
160 system is underlain by a basement confining unit which outcrops at the Ozark dome  
161 in east-central Missouri (Figure 2AC). The Ozark aquifer system (OAS) – the most  
162 important water-bearing unit of the system – crops out at the center of the system  
163 and is otherwise overlain by the Springfield Plateau aquifer system (SPAS) and/or the  
164 Western Interior Plains confining system (WIPCS). North of the Missouri - Arkansas  
165 border, carbonate-rich units such as SPAS and OAS present rich karst features (Hays  
166 et al., 2016).

167 Other aquifer systems surrounding OPAS are also shown in Figure 2. The Missis-  
168 sippi Embayment Aquifer System and the shallower Mississippi River Valley Aquifer  
169 southeast of OPAS supply much of the irrigation water for the agriculture-intensive  
170 region (Hart et al., 2008). The Mississippian Aquifers and glacial deposits from the  
171 Laurentide Ice Sheet occupy the north and northeastern boundaries of the study area  
172 (Bayless et al., 2017).

173

## 2.2 Data sets

174

### 2.2.1 Groundwater level time series

175

176

177

178

179

180

181

182

183

184

185

186

187

188

189

190

Groundwater monitoring wells (i.e., piezometers) record the temporal evolution of hydraulic head at a given depth. In this study, we take advantage of the piezometric network maintained by the United States Geological Survey which provides daily observations of water level depth (USGS Water Services; <https://waterservices.usgs.gov>). Of the 312 wells in the study area, we retain the 167 sites with 60% or more data completeness during the 2007 to 2017 timespan and further exclude seven stations classified as anomalous after visual inspection (Figure S1). For example, two time series with a typical groundwater pumping signature (Figure S1) are excluded from the analysis because these signals are expected to be very local (tens of meters) - as they represent the aquifer response to local forcings - and to bias the analysis due to their large amplitudes. We subtract the altitude at each well location to obtain the hydraulic head, detrend the time series and compute monthly averages to facilitate comparison with the other data sets used in this study. The positions of the 160 selected wells are shown in Figure 3A and examples of retained time series are presented in Figure 3B. They present seasonal and multi-annual water level oscillations from a few to tens of meters in amplitude.

191

### 2.2.2 GRACE-derived displacement time series

192

193

194

195

196

197

198

199

200

201

202

203

204

205

206

GRACE satellites monitor space and time variations in Earth's gravity field from which changes in continental water storage - which include both surface and groundwater mass (Figure 1A) - can be inferred and expressed in units of equivalent water height (EWH). At the global scale, GRACE-based models have been shown to better explain the seasonal signals in GNSS datasets than hydrology-based models (Li et al., 2016). Here, we make use of the Level 2 Release 06 spherical harmonics GRACE solution up to degree 96 where low degree harmonics  $C_{20}$  have been replaced by SLR-derived values provided by the Center for Space Research (CSR) (Bettadpur, 2018; GRACE, 2018) and DDK5-filtered to minimize north-south striping noise (Kusche et al., 2009). We add back the atmospheric and non-tidal oceanic contributions as these effects are not corrected in the GNSS data set and detrend the resulting time series. The colormap in Figure 3A shows the average annual EWH peak-to-peak amplitudes observed during the 2007 to 2017 timespan and reveals an important large-scale NW to SE gradient in regional water storage changes, with higher amplitudes concentrated around the Mississippi Alluvial Valley.

207

208

209

210

211

212

213

214

215

216

217

218

219

220

221

222

223

To quantify the large-scale hydrological elastic loading deformation resulting from changes in surface water and groundwater mass (Figure 1B), we compute the deformation expected from GRACE-inferred loads at the GNSS sites using a spherical elastic layered Earth model based on the Love number formalism (Farrell, 1972; Chanard et al., 2018). Note that while hydrological loading can, in theory, produce both elastic and viscoelastic deformation fields, here we limit our analysis to a purely elastic model given that the Earth's response is in phase with loading at the annual and multi-annual timescales. Moreover, while changes in groundwater mass do not occur exactly at the surface of the Earth, the depth at which those changes occur (on the order of 1 km at most) is negligible compared to the radius of the Earth, which is the key quantity in elastic loading equations on a spherical Earth (Farrell, 1972). For example, using a radius of 6370 km instead of 6371 km would result in a 0.01% change in the computed surface displacements. We therefore neglect this depth dependency in our calculations. Given the relatively large spatial wavelengths considered here, we also neglect the effect of relatively weak aquifer layers. Examples of the resulting time series are compared to the corresponding GNSS measurements in Figure S2. In Figure S3, we show that the modeled displacements in this region are relatively insensitive to

224 the particular choice of GRACE solution as solutions from the CSR, JPL and GFZ  
225 centers all produce displacements with mean absolute differences smaller than 1 mm  
226 (the approximate uncertainty of GNSS measurements).

### 227 **2.2.3 GNSS displacement time series**

228 GNSS tracks the vertical and horizontal displacements of geodetic monuments  
229 anchored a few meters below the ground surface (or on top of buildings for fewer than  
230 15% of stations). In this analysis, we start from the time series processed by the Nevada  
231 Geodetic Laboratory and expressed in the IGS14 reference frame (International GNSS  
232 Service), based on the latest release of the International Terrestrial Reference Frame  
233 (ITRF2014), (Altamimi et al., 2016; Blewitt et al., 2018, <http://geodesy.unr.edu>).  
234 Of the 315 stations located in the study area which is delimited by longitudes -96  
235 to -89 and latitudes 34.5 to 40.5, we retain the 92 stations with at least 60% of  
236 daily data between 2007 and 2017. After visual inspection, six additional stations  
237 (CVMS, MOGF, MOMK, MOSI, NWCC, and SAL5) are discarded due to spurious  
238 large amplitude signals. The positions of the remaining 86 stations are shown in  
239 Figures 3A and S4.

240 For each time series, we fit a trajectory model (Bevis & Brown, 2014) with a linear  
241 trend, annual and semi-annual terms and step functions to account for material changes  
242 and potential coseismic displacements (<http://geodesy.unr.edu/NGLStationPages/steps.txt>)  
243 as well as visually obvious offsets. We subtract the best-fit linear trend and step func-  
244 tions from the time series but do not correct for the periodic terms. Next, we identify  
245 and eliminate outliers defined as points that exceed three times the average deviation  
246 from the 90-day median for any of the three directions (east, north, vertical). The time  
247 series are then monthly averaged to match the GRACE temporal resolution. Finally,  
248 the spherical harmonic degree-1 deformation field is estimated from a global network  
249 of 1150 GNSS stations and subtracted from retained GNSS time series to allow for  
250 a direct comparison with GRACE observations which do not capture degree-1 mass  
251 changes (Chanard et al., 2018). Examples of the resulting time series are provided in  
252 Figure S2.

## 253 **3 Fluctuations in groundwater levels**

254 The first step towards extracting poroelastic signals from our GNSS dataset is  
255 to characterize the groundwater fluctuations responsible for the deformation. This  
256 requires some form of spatial interpolation since piezometers only probe groundwater  
257 levels at discrete points in space and are generally not co-located with GNSS sta-  
258 tions. We determine that directly interpolating between the piezometric sensors is  
259 not warranted in this case given the heterogeneous nature of aquifers and the variable  
260 depth of wells (Figure 3). For example, neighboring piezometers GW1 and GW2 in  
261 Figure 3B reveal very different temporal signatures. On the other hand, GW2 and  
262 GW3 - which are over 200 km apart - have highly correlated time series. Groundwater  
263 fluctuations at GW4 also correlate with GW2 and GW3 but are of much higher am-  
264 plitude. The groundwater dataset thus contains both regional- and local-scale signals  
265 with peak-to-peak amplitudes that span two orders of magnitude ( $\sim 0.5$  to 50 m).

### 266 **3.1 Extracting groundwater signals with ICA**

267 In light of these observations, we perform an Independent Component Analysis  
268 (ICA) on the groundwater dataset to extract the main modes of variability before  
269 proceeding with the spatial interpolation. ICA algorithms seek to recover the sta-  
270 tistically independent sources of signal assumed to generate the linearly mixed time  
271 series at each sensor (Roberts & Everson, 2001). In particular, variational Bayesian

ICA (vbICA) (Choudrey, 2002) has been shown to perform well to recover geophysical signals (e.g., postseismic, hydrology-induced and common mode error) from synthetic and real GNSS data sets (Gualandi et al., 2016; Larochelle et al., 2018). Once an independent component (IC) - i.e. a source of signal -  $i$  is isolated, it can be expressed with space and time vectors as  $IC_i = U_i S_i V_i^T$  where  $U_i$  is a normalized spatial distribution,  $S_i$  is a weighting factor and  $V_i$  is a normalized temporal function.

Figure 4 shows the temporal functions (A), weighting factors (A) and spatial distributions (B-D) obtained from a 3 components vbICA of the groundwater dataset. We use a triangulation-based natural neighbor algorithm (MATLAB, 2017) to interpolate the spatial distributions from the discrete data points (Figure 4B-D). We choose to limit our analysis to 3 components since analyses with more components (e.g., see Figure S5 for a 5 components analysis) yield similar IC1-3 and additional lower-amplitude ICs with spurious temporal functions that only explain a limited portion of data variance. The retained temporal functions all display a mix of multiannual and seasonal frequencies.

IC<sub>1</sub>, the component which explains the greatest share of data variance, has an overall positive spatial distribution and is observed at almost all wells including those outside OPAS (Figure 4B). This spatial distribution is indicative of a regional income of water linked to recharge processes (Longuevergne et al., 2007). The large fluctuations occurring in southern Missouri (e.g., at station GW4 (Figure 3)) are likely linked to the high storage capacity of thick limestone layers with limited karstification (Figure 4B). Figure S6 also reveals a crude spatial correlation between sinkhole density, which suggests a higher ability to recharge the aquifer system, and wells with high  $S_1 U_1$  values. IC<sub>2</sub> and IC<sub>3</sub> represent seasonal and multi-annual signals with different phases than IC<sub>1</sub> and exhibit heterogeneous spatial distributions with positive and negative values (Figure 4CD). These components probably compensate for local deviations from the regional behavior due to the delayed response of deeper aquifers, differing recharge and discharge mechanisms and groundwater pumping.

### 3.2 Comparing regional-scale hydrological signals across datasets

Given that IC<sub>1</sub> spans the entire study region, we expect to find a similar signal in the GRACE dataset. Performing a vbICA on the GRACE-predicted vertical displacements - completely independently from the groundwater ICA - the temporal function of the first and most important component indeed correlates very well with  $V_1^{GW}$ , as evidenced by the correlation coefficient  $\rho$  of  $-0.81$  (Figure 5A). Downward motion occurs concurrently with rising groundwater levels because GRACE-derived vertical displacements solely reflect the hydrological loading deformation due to changes in continental water storage (Figure 1B), not the poroelastic deformation (Figure 1C). The associated spatial response (Figure 5B) reflects the northwest to southeast gradient of hydrological loads.

By contrast, GNSS vertical time series should comprise both deformation fields. Performing a similar analysis on the GNSS dataset independently from the groundwater and GRACE analyses results in a lower but still significant correlation of  $\rho = -0.52$  with  $V_1^{GW}$  (Figure 5A). Note that a significant portion of GNSS stations sitting on top of OPAS were not installed until 2010 or 2011 as indicated by the grey shading in Figure 5A. Although the GNSS spatial distribution displays the same overall gradient as the GRACE-derived model with generally higher amplitudes around the Mississippi Alluvial Valley, the response is more heterogeneous (Figure 5B).

This comparison exercise demonstrates that the dominant temporal functions of all three datasets are in phase on a monthly timescale. This is consistent with a relatively uniform regional recharge of the aquifer system (Figure 4B) and with the system's karstic nature which allows for rapid communication between surface water

and groundwater (Hays et al., 2016), suggesting that the aquifer’s global behavior can be considered as unconfined. We recognize that OPAS is a complex aquifer system with both confined and unconfined units (Figure 3A) and that different hydrogeologic processes might interact to generate surface displacements. However, in this work, we choose to treat OPAS as an effectively unconfined system and infer mechanical properties under this assumption.

## 4 Poroelastic deformation

### 4.1 Hydrological elastic loading vs poroelastic eigenstrain: Insights about surface displacements from simple analytical solutions

To gain intuition about the elastic and poroelastic deformation fields we expect to find in the vicinity of an unconfined aquifer, we first develop and compare analytical solutions for surface displacements associated with the simple disk scenarios shown in Figure 1BC, assuming an elastic half-space medium. In Appendix A, we extend the poroelastic solution to an arbitrary 2D eigenstrain distribution which we later use to predict horizontal poroelastic displacements. While we rely on this elastic half-space model with an aquifer layer to analyse and model poroelastic displacements in later sections, we only show the equivalent elastic half-space loading model in this section for illustration and comparison purposes.

#### 4.1.1 Disk loading of an elastic half-space

We first consider a disk load of radius  $a$  and uniform pressure  $P$  at the surface of an elastic half-space with Young’s modulus  $E_{deep}$ , representative of hydrological loading from surface water (Figure 1B). The corresponding vertical and horizontal surface displacements were derived by Johnson (1987) and Verruijt (2009) as:

$$u_z(r) = \begin{cases} -\frac{4(1-\nu^2)}{\pi E_{deep}} Pa \mathcal{E}\left(\frac{r^2}{a^2}\right), & r \leq a \\ -\frac{4(1-\nu^2)}{\pi E_{deep}} Pr \left( \mathcal{E}\left(\frac{a^2}{r^2}\right) - \left(1 - \frac{a^2}{r^2}\right) \mathcal{K}\left(\frac{a^2}{r^2}\right) \right), & r > a \end{cases} \quad (1)$$

$$u_r(r) = \begin{cases} -\frac{(1-2\nu)(1+\nu)}{2E_{deep}} Pr, & r \leq a \\ -\frac{(1-2\nu)(1+\nu)}{2E_{deep}} P \frac{a^2}{r}, & r > a \end{cases} \quad (2)$$

where  $u_z(r)$  and  $u_r(r)$  are the vertical and horizontal displacements as a function of radial distance  $r$  and  $\mathcal{K}$  and  $\mathcal{E}$  are the complete elliptic integral of the first and second kind, respectively.

Figure 6A shows the deformation resulting from 10 km and 25 km-radius disks uniformly loaded with 5 m of water. Both the vertical and horizontal displacements extend beyond the loaded region with the maximum vertical and horizontal displacements occurring at the center of the disk and at the load boundary, respectively. Note that the amplitude of deformation is proportional to the spatial wavelength of the load.

#### 4.1.2 Poroelastic eigenstrain in a disk within an elastic half-space

Poroelastic deformation arises from dilational eigenstrains (Mura, 1982) associated with changes in pore pressure, analogous to thermoelastic deformation resulting from changes in temperature. In fact, the solutions derived here are directly applicable to the equivalent thermoelastic problem (Fleitout & Chanard, 2018). Eigenstrains refer to internal strains which, in the absence of external stresses resisting them, would



361 lead to isotropic expansion or contraction of the body. In the poroelastic case, eigen-  
 362 strains are related to changes in pore pressure,  $\Delta p$ , and hence in groundwater level,  
 363  $\Delta h$ , as:

$$\varepsilon_{eig} = \frac{\beta \Delta p (1 - 2\nu)}{E_{aq}} = \frac{\beta \rho g \Delta h (1 - 2\nu)}{E_{aq}} \quad (3)$$

364 where  $\beta$ ,  $\nu$  and  $E_{aq}$  are the Biot-Willis coefficient, Poisson's ratio and Young's modulus  
 365 of the aquifer layers, respectively, while  $\rho$  is water density and  $g$  is the gravitational  
 366 acceleration.

367 Given the relatively high hydraulic conductivity of karstified sedimentary rocks  
 368 (Domenico & Schwartz, 1998; Hays et al., 2016), in this work we assume that there is  
 369 no significant time delay between changes in pore pressure and the resulting deformation.  
 370 We also assume that deformation is entirely (poro)elastic and neglect permanent  
 371 deformation as clay minerals often responsible for inelastic processes are seldom found  
 372 in OPAS (Westerman et al., 2016).

373 Linear elastic constitutive equations accounting for eigenstrains are as follows  
 374 (Wang, 2000):

$$\varepsilon_{zz} = \frac{1}{E_{aq}} [(1 + \nu)\sigma_{zz} - \nu(\sigma_{rr} + \sigma_{\theta\theta} + \sigma_{zz})] + \varepsilon_{eig} \quad (4)$$

$$\varepsilon_{rr} = \frac{1}{E_{aq}} [(1 + \nu)\sigma_{rr} - \nu(\sigma_{rr} + \sigma_{\theta\theta} + \sigma_{zz})] + \varepsilon_{eig} \quad (5)$$

$$\varepsilon_{\theta\theta} = \frac{1}{E_{aq}} [(1 + \nu)\sigma_{\theta\theta} - \nu(\sigma_{rr} + \sigma_{\theta\theta} + \sigma_{zz})] + \varepsilon_{eig} \quad (6)$$

375 Given that lateral motion is restrained by the elastic medium below, it can be  
 376 shown that horizontal strains within the aquifer layers,  $\varepsilon_{rr}$  and  $\varepsilon_{\theta\theta}$ , although not  
 377 strictly null, are negligible compared to  $\varepsilon_{eig}$  in this case (Fleitout & Chanard, 2018).  
 378 Under this assumption, lateral stresses,  $\sigma_{rr}$  and  $\sigma_{\theta\theta}$ , can be approximated as:

$$\sigma_{rr} = \sigma_{\theta\theta} = \frac{-E_{aq}\varepsilon_{eig} + \nu\sigma_{zz}}{1 - \nu} \quad (7)$$

379 where  $\sigma_{zz}$  is the change in total vertical stress associated with a change in groundwater  
 380 level  $\Delta h$ :

$$\sigma_{zz} = -\phi\rho g\Delta h \quad (8)$$

381 where  $\phi$  is the porosity of the aquifer layers and the negative sign indicates compressive  
 382 stresses. Substituting Equations (3), (7) and (8) into (4) and integrating the vertical  
 383 strain over the saturated aquifer thickness  $b$  and radius  $a$  yields the following vertical  
 384 deformation field at the surface:

$$u_{z,exp}(r) = \begin{cases} \frac{(1 + \nu)(1 - 2\nu)(\beta - \phi)\rho g\Delta h(r)b}{(1 - \nu)E_{aq}}, & r \leq a \\ 0, & r > a \end{cases} \quad (9)$$

385 Here we must integrate over the entire saturated thickness  $b$  since pore pressure in-  
 386 creases over the entire depth of the hydraulically-connected aquifer when it is recharged  
 387 with additional water. Equation (9) describes the vertical poroelastic expansion of the  
 388 aquifer layers in excess of the elastic loading deformation resulting from the added  
 389 groundwater load ( $\phi\rho g\Delta h$ ) within these elastically weak layers.

390 The total horizontal strain, sum of the elastic and eigenstrain, has to be small  
 391 compared to the eigenstrain because it requires deformation of the elastic medium  
 392 below the aquifer. In fact, compensation of horizontal eigenstrain by elastic strain

requires strong variations in lateral stress  $\sigma_{rr}$  within the aquifer (Equation (7)). These variations in  $\sigma_{rr}$  necessarily induce shear stresses at the base of the aquifer, which results in both horizontal and vertical displacements within the medium below the aquifer. We can see this effect by solving for this basal shear stress,  $\sigma_{rz}(z = b)$ , considering the stress equilibrium equations for an axisymmetric problem in cylindrical coordinates:

(Wang, 2000):

$$\frac{\partial \sigma_{rz}}{\partial r} + \frac{\partial \sigma_{zz}}{\partial z} + \frac{\sigma_{rz}}{r} = 0 \quad (10)$$

$$\frac{\partial \sigma_{rz}}{\partial z} + \frac{\partial \sigma_{rr}}{\partial r} + \frac{\sigma_{rr} - \sigma_{\theta\theta}}{r} = 0 \quad (11)$$

Substituting Equation (7) into (11), integrating with respect to  $z$  and applying a zero shear stress boundary condition at the surface ( $\sigma_{rz}(z = 0) = 0$ ) yields:

$$\sigma_{rz}(z = b) = - \int_0^b \frac{\partial}{\partial r} \left[ \frac{-E_{aq}\varepsilon_{eig} + \nu\sigma_{zz}}{1 - \nu} \right] \partial z \quad (12)$$

$$= \frac{\partial}{\partial r} I(r) \quad (13)$$

where

$$I(r) = \int_0^b \frac{E_{aq}\varepsilon_{eig} - \nu\sigma_{zz}}{1 - \nu} \partial z \quad (14)$$

is the fundamental quantity driving poroelastic deformation (Fleitout & Chanard, 2018). For the simple disk aquifer considered here,  $E_{aq}$ ,  $\varepsilon_{eig}$ ,  $\nu$  and  $\sigma_{zz}$  are uniform within the aquifer and  $\varepsilon_{eig}$  and  $\sigma_{zz}$  are equal to zero outside the aquifer such that:

$$I(r) = \frac{(E_{aq}\varepsilon_{eig} - \nu\sigma_{zz})b}{1 - \nu} \mathcal{H}(a - r) \quad (15)$$

$$= \frac{(\beta(1 - 2\nu) + \phi\nu)\rho g \Delta h b}{(1 - \nu)} \mathcal{H}(a - r) \quad (16)$$

$$= I_{disk} \mathcal{H}(a - r) \quad (17)$$

and

$$\sigma_{rz}(z = b) = I_{disk} \delta(r - a) \quad (18)$$

where  $\mathcal{H}$  and  $\delta$  are the Heaviside and Dirac delta functions, respectively. Finally, we predict the deformation induced by  $\sigma_{rz}(z = b)$  with the expressions derived by Johnson (1987) for surface displacements due to an axisymmetric shear stress distribution,  $q(t)$ :

$$u_{z, shear}(r) = \begin{cases} -\frac{(1 - 2\nu)(1 + \nu)}{\pi E_{deep}} \int_r^a q(t) dt, & r \leq a \\ 0, & r > a \end{cases} \quad (19)$$

$$u_{r, shear}(r) = \frac{4(1 - \nu^2)}{\pi E_{deep}} \int_0^a \frac{t}{t + r} q(t) \left[ \left( \frac{2}{k^2} - 1 \right) \mathcal{K}(k) - \frac{2}{k^2} \mathcal{E}(k) \right] dt \quad (20)$$

where  $k^2 = 4tr/(t + r)^2$ . Using  $\sigma_{rz}(z = b)$  as  $q(t)$ , inclusive limits of integration and the sifting property of the Dirac delta function results in:

$$u_{z, shear}(r) = \begin{cases} -\frac{(1 - 2\nu)(1 + \nu)}{\pi E_{deep}} I_{disk}, & r \leq a \\ 0, & r > a \end{cases} \quad (21)$$

$$u_{r, shear}(r) = \frac{4(1 - \nu^2)}{\pi E_{deep}} I_{disk} \frac{a}{a + r} \left[ \left( \frac{2}{k^2} - 1 \right) \mathcal{K}(k) - \frac{2}{k^2} \mathcal{E}(k) \right] \quad (22)$$

where  $k^2 = 4ar/(a+r)^2$ . At  $r = a$ ,  $u_{r, shear}$  has an infinite value. Our mathematical framework is derived in a “thin layer” approximation, and therefore only valid for spatial wavelengths larger than the aquifer thickness. It would be possible to derive analytical solutions in a more complex mathematical framework for shorter wavelengths. However, for simplicity, we choose to numerically approach the diverging solution of Equation (22) at  $r = a$  by truncating its expansion series (Appendix B), which has no impact at distances larger than the aquifer thickness.

To obtain an order of magnitude estimate of the poroelastic displacements expected in OPAS, we compute the poroelastic deformation generated by a 20 m increase in groundwater level in unconfined disk aquifers with radii of 10 km and 25 km and a thickness of 1000 m (Figure 6B). These parameter values are representative of the localized zone of elevated groundwater variations observed at the center of OPAS (Figure 4B) and are consistent with the equivalent elastic loading scenarios shown in Figure 6A, assuming a porosity of 25%. The vertical displacement is largely due to poroelastic expansion and is bounded by the aquifer. The horizontal poroelastic displacement, on the other hand, is entirely due to the shear stress imposed at the base of the aquifer and extends beyond the aquifer. Moreover, the amplitude of deformation is independent of the wavelength of pore pressure perturbation in contrast to the hydrological loading case. Indeed, the 10 and 25 km disks result in displacements of the same amplitude. In fact, expressions for horizontal displacements given by Equations (2) and (22) become independent of the disk radius  $a$  when evaluated for distances  $r = r/a$ . We rely on the observation that poroelastic displacements only depend on local changes in pore pressure to justify the use of elastic half-space models - as opposed to a spherical Earth model - for the upcoming analysis.

## 4.2 Extraction of geodetic poroelastic displacements

In order to extract poroelastic deformation from GNSS time series, we first assume that deformation from hydrological loading is well reproduced by the GRACE model and hence focus on the GNSS - GRACE residual time series. This assumption is supported by a comparison of the vertical time series in Figures 7 and S2. The geodetic deformation at station ZKC1 located outside OPAS and other aquifer systems (Figure 3A) is well explained by the GRACE model and presents very little residual seasonal displacements (Figure 7A). This is consistent with Chanard et al. (2018)’s finding that vertical displacements observed by GNSS are generally well explained by a GRACE loading model at a global scale because most stations are located at bedrock sites. At station MOWS at the center of OPAS, on the other hand, the GNSS vertical displacements deviate from that predicted from loading effects and the residuals show clear seasonal and multiannual features (Figure 7B).

For the horizontal components, we first estimate and remove the common mode deformation from the GNSS-GRACE residual time series to isolate OPAS’s poroelastic response. We estimate the common mode by taking a spatial average of all horizontal GNSS-GRACE residual time series within the study area. This step is necessary as Figure S7 illustrates that neighbouring aquifers can induce significant horizontal poroelastic deformation within the study region. Although the horizontal displacements in OPAS caused by the synthetic poroelastic eigenstrains in Figure S7D are affected by boundary effects and vary with distance from the perturbed zone, most stations do move in the same direction, similar to the displacements extracted through our methodology but without removing the common mode (Figure S7C). Subtracting the common mode from GNSS-GRACE residual time series should thus account for the first order effects of neighbouring aquifers.

We posit that at least part of these seasonal and multiannual residuals can be attributed to instantaneous poroelastic deformation and should therefore be propor-

464 tional to and in phase with groundwater fluctuations. Since we know the dominant  
 465 temporal functions that make up the groundwater fluctuations, we can test this hy-  
 466 pothesis by projecting the residual geodetic time series onto these functions. However,  
 467 unlike the related Principal Component Analysis (PCA) technique, ICA yields inde-  
 468 pendent components which are not constrained to be orthogonal. Before proceeding  
 469 with the projection, we must thus orthogonalize vectors  $V_1^{GW}$ ,  $V_2^{GW}$  and  $V_3^{GW}$  from  
 470 Section 3.1 via the Gram-Schmidt process to produce an orthogonal basis, enabling us  
 471 to sum the contribution of each basis vector as follows:

$$P_j = \frac{R_j \cdot W_1}{\|W_1\|^2} W_1 + \frac{R_j \cdot W_2}{\|W_2\|^2} W_2 + \frac{R_j \cdot W_3}{\|W_3\|^2} W_3 \quad (23)$$

472 where  $P_j$  is the inferred poroelastic displacement for direction  $j$  (i.e., east, north or up),  
 473  $R_j$  is the GNSS-GRACE residual time series and  $W_1, W_2, W_3$  are the orthogonalized  
 474 versions of  $V_1^{GW}, V_2^{GW}, V_3^{GW}$ . Figure S8 reveals that the  $V_i^{GW}$ 's were not far from  
 475 orthogonality to start with since  $W_2$  and  $W_3$  only differ marginally from  $V_2^{GW}$  and  
 476  $V_3^{GW}$ , respectively.

477 The resulting  $P_j$ 's are shown in yellow in Figure 7 and Figure S2. The recovered  
 478 vertical poroelastic deformation is relatively small at station ZKC1 outside of  
 479 aquifer systems and relatively large at station MOWS at the center of OPAS. How-  
 480 ever, both stations exhibit similar amplitudes of horizontal poroelastic deformation.  
 481 This behavior is consistent with the analytical solutions developed in Section 4.1.

### 482 4.3 Vertical poroelastic displacements

483 Figure 8 illustrates the amplitudes of the poroelastic signals extracted with each  
 484 groundwater temporal function  $W_i$ . Similar to the groundwater spatial distributions  
 485 in Figure 4, the vertical poroelastic signal recovered with  $W_1$  is mostly positive and is  
 486 more extensive and of higher amplitude than the signals recovered with  $W_2$  and  $W_3$ .  
 487 The poroelastic signals associated with  $W_2$  and  $W_3$  present both positive and negative  
 488 values like the  $S_2U_2$  and  $S_3U_3$  distributions of groundwater.

489 Focusing on this regional signal, Figure 8A shows that many stations outside  
 490 OPAS exhibit amplitudes comparable to those inside OPAS. We attribute these poroe-  
 491 lastic displacements to the other major aquifer systems present in the region (Figure  
 492 2). Westernmost stations (e.g., ZKC1) where major aquifer structures are sparse or  
 493 non-existent display some of the smallest amplitudes. However, it is difficult to eval-  
 494 uate whether or not a GNSS station is sitting on top of an aquifer system since the  
 495 map in Figures 2 and S4 only indicates the surface outcrops of these aquifer systems.  
 496 The particularly large seasonal displacements at station OKMU (Figure S2C) at the  
 497 southwestern edge of OPAS might be due to intensive groundwater pumping. Unfortu-  
 498 nately there is no nearby groundwater monitoring well active during this time period  
 499 to test this hypothesis. Finally, as Eq. (9) suggests, the range of vertical poroelastic  
 500 amplitudes observed within OPAS - from about 2 to 14 mm - may reflect differences in  
 501 poroelastic ( $\beta$ ,  $\phi$ ,  $E_{aq}$ ) properties, groundwater variations ( $\Delta h$ ) or saturated aquifer  
 502 thickness ( $b$ ). We discuss this further in Section 5.

### 503 4.4 Horizontal poroelastic displacements

504 As for horizontal displacements, Figure 8D-F suggests that all three temporal  
 505 functions  $W_i$ 's are associated with spatially heterogeneous poroelastic deformation on  
 506 the order of a few millimeters. According to Equation (22), poroelastic horizontal  
 507 displacements are governed by deep elastic parameters as opposed to the aquifer prop-  
 508 erties relevant for vertical poroelastic expansion. Elastic properties are believed to  
 509 be more laterally homogeneous at depth than at the surface. Indeed, as discussed in  
 510 Section 5.2, surficial layers are more prone to fracturing which can alter elastic moduli.  
 511 We thus approximate  $E_{deep}$  with a constant value of 80 GPa and use Equations (A3)

512 and (A4) for a spatially variable 2D distribution  $I(x, y)$  (A1) to predict the horizontal  
513 poroelastic deformation induced by the observed groundwater fluctuations.

514 The colormaps in Figure 8D-F show the spatial distributions of  $I(x, y)$  interpo-  
515 lated within OPAS for each groundwater IC as well as the resulting displacements  
516 at the GNSS sites (red arrows). Although the model predictions associated with  $W_1$   
517 match the observed displacements to first order at a handful of stations within OPAS,  
518 the observations are more heterogeneous than predicted (Figure 8D). For example,  
519 station MOBW undergoes a 7 mm displacement to the southwest whereas the model  
520 predicts a sub-millimetric eastward displacement (Figure S2D). The models for  $W_2$   
521 and  $W_3$ , on the other hand, fail to match the extracted displacements (Figure 8EF).

522 There are a number of potential reasons for these discrepancies. First and fore-  
523 most, horizontal poroelastic displacements are highly sensitive to local variations in  
524 groundwater levels since they depend on the gradient of the groundwater field (e.g.,  
525 Equation (13)) and do not attenuate with decreasingly small perturbation wavelengths.  
526 Hence, the spatial resolution of the piezometric network might be insufficient to accu-  
527 rately model the horizontal deformation. One way to improve the analysis would be to  
528 refine the spatial resolution of surface deformation measurements using InSAR (with  
529 the caveat that InSAR is mostly sensitive to east-west and vertical deformation). The  
530 model could also be extended to account for perturbation wavelengths smaller than  
531 the thickness of the aquifer. Some of the large horizontal displacements might also  
532 be due to hydrogeologic phenomena not included in the present model. For example,  
533 Silverii et al. (2016) and Serpelloni et al. (2018) explain horizontal transient signals  
534 observed around karstic aquifers with the opening and closing of vertical tensile dis-  
535 locations due to groundwater variations. Groundwater pumping and the associated  
536 cones of depression might also be inducing horizontal deformation within the aquifer  
537 system itself (Helm, 1994).

538 Finally, our projection methodology might be capturing sources of seasonal and  
539 multi-annual signals not associated with groundwater. In particular, Fleitout & Cha-  
540 nard (2018) show that important horizontal thermoelastic displacements can result  
541 from sharp variations in elastic properties. Heterogeneities in hydrological loading  
542 from surface water not captured by GRACE might also be responsible for some of the  
543 discrepancy. However, this would require relatively strong heterogeneities in surface  
544 water variations since, as demonstrated in Figure 6A and as opposed to poroelastic  
545 deformation, the amplitude of deformation associated with hydrological elastic load-  
546 ing decreases with decreasing load size. In the next section, we present a preliminary  
547 analysis to quantify the displacements induced by surface hydrological fluctuations not  
548 detected by GRACE.

#### 549 4.5 Hydrological loading from small-scale surface water heterogeneities

550 As the GRACE model only captures long-wavelength hydrological loads, our  
551 GNSS-GRACE residuals may contain signals from small-scale hydrological surface  
552 loads in addition to groundwater-related deformation. Thoroughly quantifying the  
553 role of these small-scale heterogeneities in GNSS time series would require a sufficiently  
554 resolved spatiotemporal characterization of surface water variations throughout OPAS.  
555 We can, however, assess how important this effect is in our study area by considering  
556 the illustrative case of the Harry S. Truman Reservoir in central Missouri for which we  
557 have a record of the water levels ([https://waterdata.usgs.gov/nwis/dv?referred\\_module=sw&site\\_no=06922440](https://waterdata.usgs.gov/nwis/dv?referred_module=sw&site_no=06922440)) (Figure 9AB). If fluctuations in the lake reservoir  
558 were causing important solid Earth deformation, we would expect that projecting  
559 GNSS-GRACE residuals of nearby stations onto the water level time series would  
560 result in significant projection signals, similar to the poroelastic case. In the case  
561

of vertical displacements, we would also expect the recovered signal to be in phase opposition with the water levels given the elastic loading nature of the deformation.

However, Figure 9CD reveals that performing such a projection at nearby stations MOCL and MOWW results in vertical signals of relatively small amplitudes and in phase with water levels. As for the horizontals, we do find a significant signal in the north component of station MOWW. The fact that the recovered signal is in phase with the groundwater projection suggests that the residuals could be due to elastic loading from the reservoir, poroelastic effects or a mix of both.

We can also use the analytical model from Section 4.1.1 to compute the elastic loading displacements expected from water level variations in the Truman Reservoir. In Figure 9E, we show that the displacements expected from a 5 m increase in water level over a circular region of radius 1.5 km - representative of the small portion of the Truman Reservoir closest to station MOCL - are below the 1 mm threshold of GNSS accuracy. Using a circular region with the same total surface area as that of the reservoir, on the other hand, does result in significant millimetric displacements at both stations MOWW and MOCL (Figure 9F). If the north displacements at station MOWW were indeed caused by elastic loading from the Truman reservoir, Figure 9F suggests that we should observe even larger displacements in the vertical direction. Since this is not what we observe in Figure 9D, we conclude that elastic loading from the Truman reservoir must be relatively small compared to the poroelastic effect. Although this analysis is limited to a single reservoir due to the paucity of water level data, we assume these findings to be representative of other lakes and reservoirs in the study area.

## 5 Aquifer mechanical properties

### 5.1 Estimating aquifer elastic parameters from vertical geodetic measurements

As discussed in Section 4, vertical poroelastic displacement is primarily due to the expansion and contraction of aquifer layers in response to groundwater fluctuations. Assuming that the system is effectively unconfined and that the ICs extracted in Section 3 indeed capture the groundwater variations responsible for the poroelastic deformation, we can estimate an effective aquifer Young modulus  $E_{aq}$  directly below each GNSS station by rearranging Eq. (9) as:

$$E_{aq} = \frac{(1 + \nu)(1 - 2\nu)}{(1 - \nu)} \frac{(\beta - \phi)\rho g \Delta h b}{u_{z,exp}} \quad (24)$$

To this end, we compare the interpolated groundwater fluctuations from Section 3 to the inferred vertical poroelastic deformation from Section 4. Note that  $E_{aq}$  only depends on the vertical displacement in Eq. (24) and, as such, poroelastic horizontal displacements are not used in constraining the elastic modulus. For each GNSS station where both datasets are available, we consider the slope and coefficient of determination,  $R^2$ , of the best-fit line through the displacement vs groundwater level space (Figure S9). The slope represents the ratio of vertical displacement to groundwater variation,  $u_{z,exp}/\Delta h$ , whose inverse enters Eq. (24) and  $R^2$  quantifies the fit of the linear regression. The higher  $R^2$  is, the more correlated the two datasets are and, hence, the more confident we are in the  $E_{aq}$  estimate. Figure 10A shows examples of vertical displacement and groundwater level time series with different  $R^2$  values and Figure 10B illustrates the spatial distribution of  $R^2$ . We only retain stations with  $R^2 > 0.35$  such as MOC3, ARBT and MOSD to estimate  $E_{aq}$ . Station ARHR illustrates a case where the time series are too incoherent to infer a meaningful value of  $E_{aq}$ . Stations with low  $R^2$  might reflect localities where spatial interpolation of the groundwater ICs fails to reproduce the actual variations in groundwater levels. For example, station

ARHR and two of its neighbours which also display low  $R^2$  values are all located in a region with relatively few piezometric measurements.

For the thickness  $b$ , we assume that there is significant hydraulic connectivity between the different aquifer units making up OPAS (as evidenced by the temporal correlation in Figure 5A) and sum their thicknesses. We also assume that the aquifer is saturated over its entire thickness. Figure 10C shows the total thickness,  $b_{model}$ , derived from Westerman et al. (2016)'s hydrogeological model. We extrapolate this thickness distribution for GNSS stations that are within 0.2 of the OPAS surface trace. Assuming representative constant values of  $\nu = 0.25$ ,  $\beta = 0.80$ , and  $\phi = 0.25$  (Domenico & Schwartz, 1998), we obtain estimates of  $E_{aq}$  at the 30 retained sites where all three datasets ( $\Delta h$ ,  $b_{model}$  and  $u_{z,exp}$ ) are available (Figure 10D). We also interpolate between stations given that the vertical poroelastic field is governed by the relatively homogeneous spatial distribution associated with  $W_1$  (Figure 8A). Figure 11 reveals that this (preferred) distribution of  $E_{aq}$  mostly falls between 1 and 10 GPa. We discuss these values further in Section 5.2.

## 5.2 Explaining low field estimates of $E_{aq}$

In Section 5.1 we estimated a distribution for  $E_{aq}$  with values ranging from 0.04 to 18 GPa and a median of 1.58 GPa (Figure 11). These values are lower than the laboratory-constrained elastic moduli of the principal rocks found in OPAS: limestone, dolomite, sandstone and shale (Westerman et al., 2016). For example, Ge & Garven (1992) suggest values of 125, 68, 9 and 11 GPa for the Young modulus of Blair Dolomite, Maxville Limestone, Berea Sandstone and Chattanooga Shale, respectively (see Table S1), pointing to an average Young modulus of the order of 50 GPa.

Here we investigate whether this order of magnitude discrepancy could be due to uncertainties on the various parameters involved in estimating  $E_{aq}$ . We evaluate the uncertainty on parameter  $b$  at  $\pm 36$  m based on the root mean square errors reported by Westerman et al. (2016). For the poroelastic constants, Domenico & Schwartz (1998) states that the Poisson ratio  $\nu$  falls within 0.25 and 0.33 for most rocks and that the porosity  $\phi$  of limestone (including karst limestone), dolomite, sandstone and shale ranges from 0 to 0.40. As for the Biot-Willis coefficient  $\beta$ , we infer a range of 0.60 to 0.90 based on the reported values of 0.69, 0.76 and 0.95 for limestone, sandstone and mudstone, respectively (Domenico & Schwartz, 1998).

We then compute the minimum and maximum expected distributions of  $E_{aq}$  in Figure 11 by considering the parameter values within these uncertainty ranges that minimize and maximize the factor  $(1+\nu)(1-2\nu)/(1-\nu)(\beta-\phi)b$  in Equation (24). The medians of the resulting distributions are 0.43 and 2.73 GPa, respectively. Since the maximum estimated values of  $E_{aq}$  are still generally an order of magnitude smaller than those observed in the laboratory, we argue that there is a robust discrepancy between elastic modulus measured at these different scales.

Lower-than-expected elastic modulus cannot be explained by the potential underestimation of hydrological loading displacements associated with small-scale heterogeneities in surface water discussed in Section 4.5. Indeed, if the loading deformation is underestimated by GRACE, the vertical poroelastic response would be underestimated as well and hence the Young modulus would be overestimated. This is because vertical poroelastic and elastic loading displacements act in opposite directions. For example, if the actual loading induces a -5 mm deformation and the poroelastic displacement is 10 mm, GNSS would record a net signal of 5 mm (since  $GNSS = \text{poroelastic} + \text{loading}$ ). Now if GRACE underestimates the loading deformation at -3 mm instead of -5 mm, we would underestimate the poroelastic signal at 8 mm instead of 10 mm and, thus, overestimate the Young modulus.

660 There is, however, a growing body of evidence that laboratory-based values over-  
 661 predict *in situ* estimates of effective elastic moduli (e.g., Matonti et al., 2015; Bailly et  
 662 al., 2019). Matonti et al. (2015), for instance, report seismic velocities,  $V_p$ , measured  
 663 on carbonate rock outcrops that are up to 70% smaller than those obtained on rock  
 664 samples in the laboratory, implying a tenfold reduction in elastic moduli. Although  
 665 part of the discrepancy is probably due to the greater porosity observed in the field  
 666 (e.g., due to karstic features in this case), Fortin et al. (2007) and Bailly et al. (2019)  
 667 have shown that seismic velocities - and hence elastic moduli - are more sensitive to  
 668 geological features with high aspect ratios such as cracks, fractures, bedding plane and  
 669 faults because they are more compliant to deformation than spherical pores.

670 Following the effective medium theory framework of Fortin et al. (2007), the ratio  
 671 of effective bulk modulus  $K$  to bulk modulus of the intact rock,  $K_o$ , can be described  
 672 in terms of porosity,  $\phi$ , and fracture density,  $f$ , defined as  $f = Nc^3/V$ , where  $N$  is  
 673 the number of penny-shaped cracks with radius  $c$ , embedded in a volume  $V$  (Walsh,  
 674 1965):

$$\frac{K_o}{K} = 1 + \frac{3}{2} \frac{(1 - \nu_o)}{(1 - 2\nu_o)} \phi + \frac{16}{9} \frac{(1 - \nu_o^2)}{(1 - 2\nu_o)} f \quad (25)$$

675 where  $\nu_o$  is the Poisson ratio of the intact rock. Assuming  $\nu_o = 0.25$ , Eq. (25) reduces  
 676 to:

$$\frac{K_o}{K} = 1 + 2.25\phi + 3.33f \quad (26)$$

677 Thus, a fourfold reduction in elastic modulus ( $K_o/K = 4$ ) for example would  
 678 require - assuming a spherical pore porosity of 25% - a fracture density  $f$  of 0.7, a  
 679 common value reported in fractured reservoirs (Bailly et al., 2019). We thus conclude  
 680 that the reduction in elastic moduli is mostly due to the presence of fracture-like  
 681 geological features as in previous studies (Matonti et al., 2015; Bailly et al., 2019).

## 682 6 Conclusions

683 To summarize, in this study, we characterized the spatiotemporal variations of  
 684 OPAS's groundwater levels with three independent components. In particular, we un-  
 685 covered a regional-scale groundwater signal that is temporally correlated with geodetic  
 686 observations. Then, by assuming that large-scale hydrological loading displacements  
 687 are well described by a GRACE-based model and that poroelastic deformation is in  
 688 phase with groundwater fluctuations, we extracted vertical and horizontal poroelas-  
 689 tic displacement fields from GNSS time series by projecting onto the groundwater  
 690 temporal functions. We also quantified the amplitudes of displacements induced by  
 691 hydrological loading vs poroelastic effects with analytical solutions and developed a 2D  
 692 poroelastic model to relate groundwater perturbations in an unconfined aquifer system  
 693 to surface displacements. Finally, we found that the extracted groundwater variations  
 694 and vertical poroelastic displacements imply an heterogeneous spatial distribution of  
 695 Young modulus with values no larger than a few GPa's.

696 Our findings have important implications in the fields of hydrology, geodesy and  
 697 seismology. First, the excellent correlation between the GRACE and groundwater  
 698 temporal functions indicates that there is consistency between the water mass fluctua-  
 699 tions observed at the local and continental scales. Filtering groundwater levels dataset  
 700 with ICA could also lead to improved piezometric maps free of aberrant local signals.  
 701 In terms of poroelastic displacements, the OPAS example clearly demonstrates that  
 702 both hydrological loading and poroelastic effects can induce significant geodetic defor-  
 703 mation in the vertical and horizontal directions - hence the need to account for both  
 704 deformation fields when correcting GNSS time series for hydrological effects. Since the



705 two types of deformation can interfere destructively, failing to account for poroelastic  
706 effects in hydrogeodetic inversions could result in large errors in estimates of total  
707 water storage variations. The notion that poroelastic stresses may be locally stronger  
708 than those generated from hydrological loading (due to their relative amplitudes at  
709 small perturbation wavelengths) also warrants revisiting the role of both sources of  
710 stress in triggering seasonal seismicity (Craig et al., 2017). Lastly, our relatively low  
711 geodetic estimates of Young modulus motivates further investigation into surficial elastic  
712 parameters and their effect on global hydrological loading models (Chanard et al.,  
713 2018).

714 While this study is clarifying the signature of large aquifer systems in GNSS  
715 time series, further work is certainly necessary to address the current limitations of  
716 our methodology, starting with testing the validity of the method in other aquifer  
717 settings. In particular, the methodology should be evaluated in non-karstic and/or  
718 confined aquifer environments as well as in systems undergoing inelastic deformation.  
719 Furthermore, the poroelastic model presented here neglects horizontal strains within  
720 the aquifer layers which may be more important in confined systems. We also recognize  
721 that the signals we attribute to poroelastic origins may be contaminated by other  
722 sources of seasonal signals, either due to deformation from thermal, atmospheric and  
723 residual hydrological loading effects or to systematic errors in the GRACE and GNSS  
724 data processing. Chanard et al. (2020) report draconitic signals, aliasing from mismod-  
725 elled tides, tropospheric delays and other environmental effects as potential sources of  
726 seasonal noise and systematic errors in GNSS datasets. Perhaps most importantly, our  
727 work suggests that horizontal poroelastic displacements are highly sensitive to spatial  
728 variations in groundwater, making it difficult to accurately extract them from GNSS  
729 time series without a sufficient resolution of the piezometric surface.

730 Future work will thus focus on characterizing the horizontal deformation field  
731 that would help identify possible local effects in the vicinity of groundwater monitoring  
732 wells using InSAR displacement time series. Accurately measuring aquifer deformation  
733 is essential to understand its mechanics at the system scale, which is not possible  
734 from piezometric monitoring alone given the hydromechanical couplings involved. In  
735 particular, a more complete characterization of surface horizontal displacements should  
736 lead to an improved understanding of how water is stored in the different aquifers units  
737 of the Ozark system (confined-unconfined) as well as their connections.

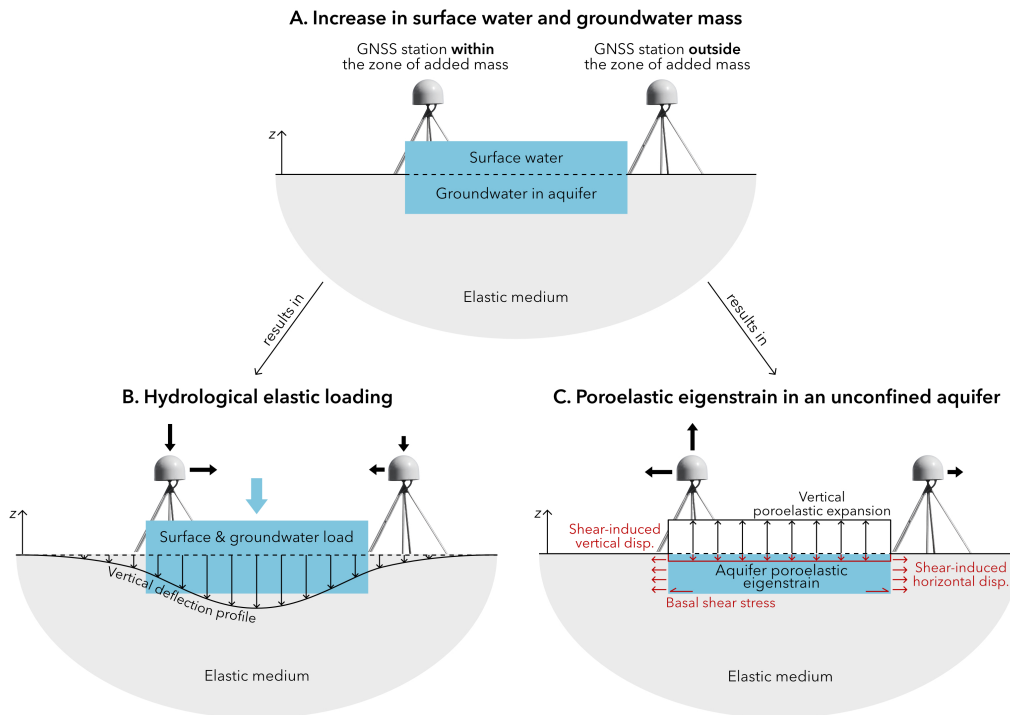


**Figure 1: Deformation due to hydrological elastic loading vs poroelastic eigenstrain.** **A.** Schematic representation of an increase in surface and groundwater mass in the vicinity of GNSS stations. **B.** The added mass, whether at the surface or in the ground, causes subsidence and horizontal motion towards the added load. The surface vertical displacement expected from a circular load on an elastic half-space is shown in black. **C.** At the same time, groundwater recharge increases pore water pressure within the aquifer, leading to upward vertical and outward horizontal displacements. While most of the vertical deformation comes from poroelastic expansion (black), horizontal and vertical displacements also result from basal shear stresses (red).

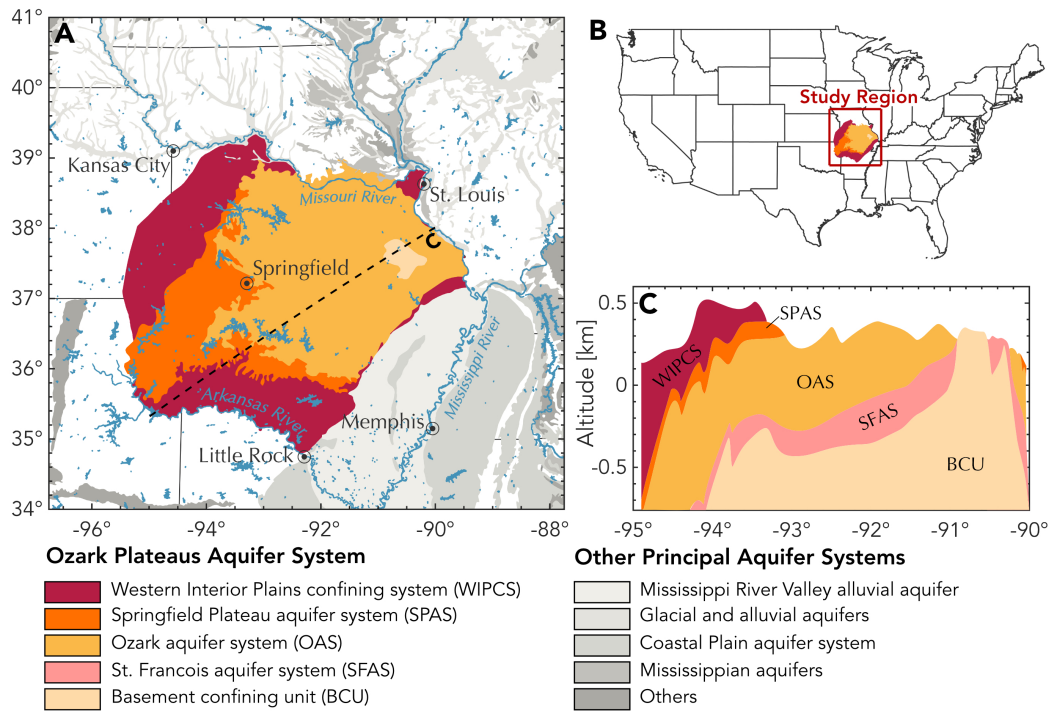


**Figure 2: Regional hydrogeological setting.** **A.** Simplified outcrop map of the Ozark Plateaus Aquifer System (OPAS) based on physiographic sections (modified from Hays et al. (2016) and Knierim et al. (2017)) and neighbouring aquifer systems (from USGS map of Principal Aquifers). **B.** Geographical location of OPAS. **C.** Hydrogeological cross-section at the dashed line in A based on Westerman et al. (2016).

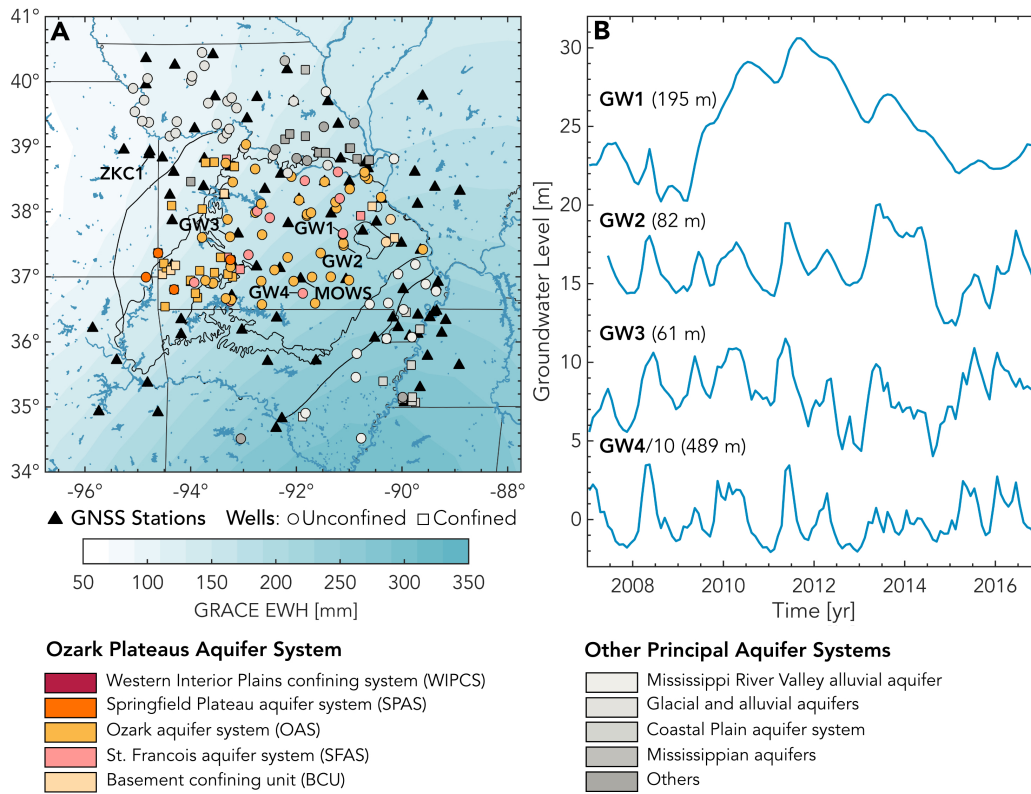


**Figure 3: GNSS, GRACE and groundwater data sets.** **A.** Annual EWH peak-to-peak amplitudes derived from GRACE and locations of GNSS stations and groundwater monitoring wells used in this study. The color of the well markers indicates the aquifer system at the base of a well and the shape describes the type of aquifer(s) - i.e., confined or unconfined - encountered by a well (as classified by the USGS). **B.** Example of groundwater time series at different locations across OPAS. Note that the time series are offsetted and that GW4 is divided by a factor of 10 for illustration purposes. Well depths are indicated in parenthesis. The featured wells correspond to USGS site numbers 373955091065901 (GW1), 372853091061801 (GW2), 373701093151601 (GW3) and 364324091515001 (GW4).

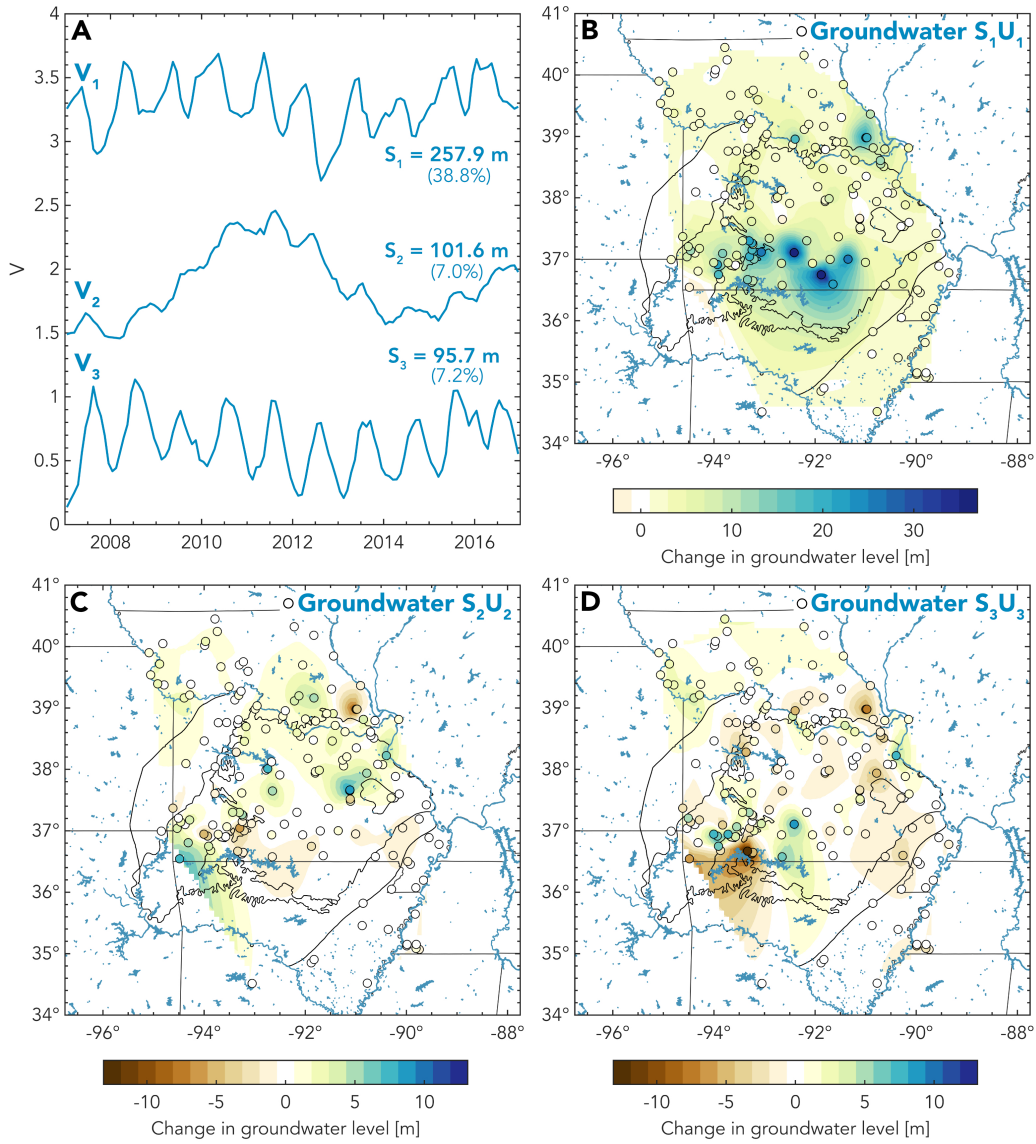


**Figure 4: ICA decomposition of the groundwater dataset.** **A.** Temporal evolution and weighting factors of the three components ICA. The temporal functions are offsetted for illustration purposes. The variance of the groundwater dataset explained by each component is also indicated in parenthesis. **B-D** Weighted spatial distributions of the three components (circles). Spatial interpolation of the distributions is also shown.

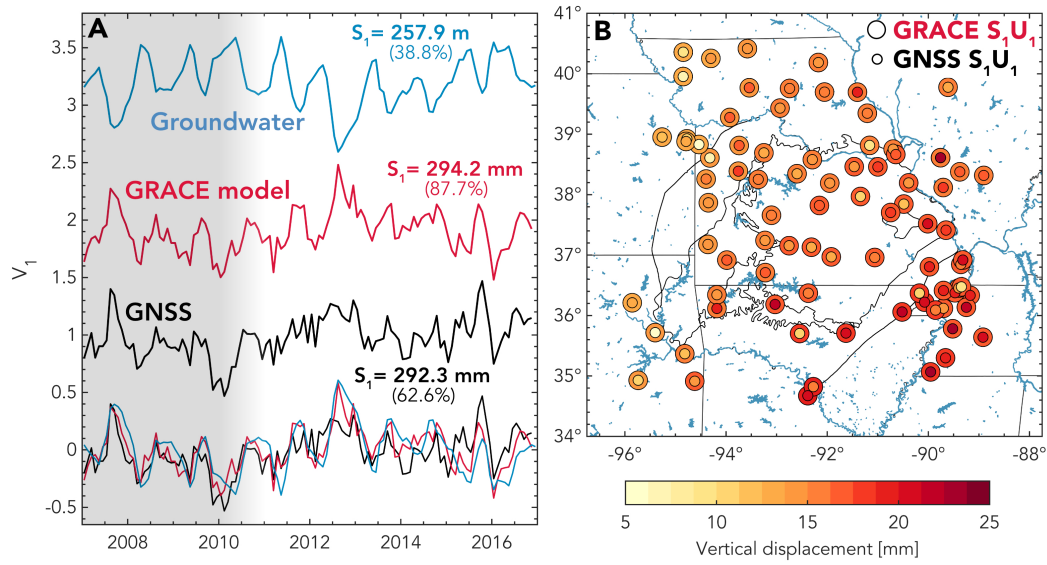


**Figure 5: Temporal correlation between the first independent component of groundwater and the GRACE-predicted and GNSS vertical displacements. A.** Temporal functions (offsetted), weighting factor and variance explained for each dataset. The 3 temporal functions are replotted at the bottom of the figure (note that the groundwater function is flipped) to facilitate visual comparison. The grey shaded area indicates the timespan prior to the installation of most GNSS stations sitting on top of OPAS from 2010 to 2011. **B.** Spatial distribution of the GRACE-predicted (outer circles) and GNSS (inner circles) vertical displacement datasets.

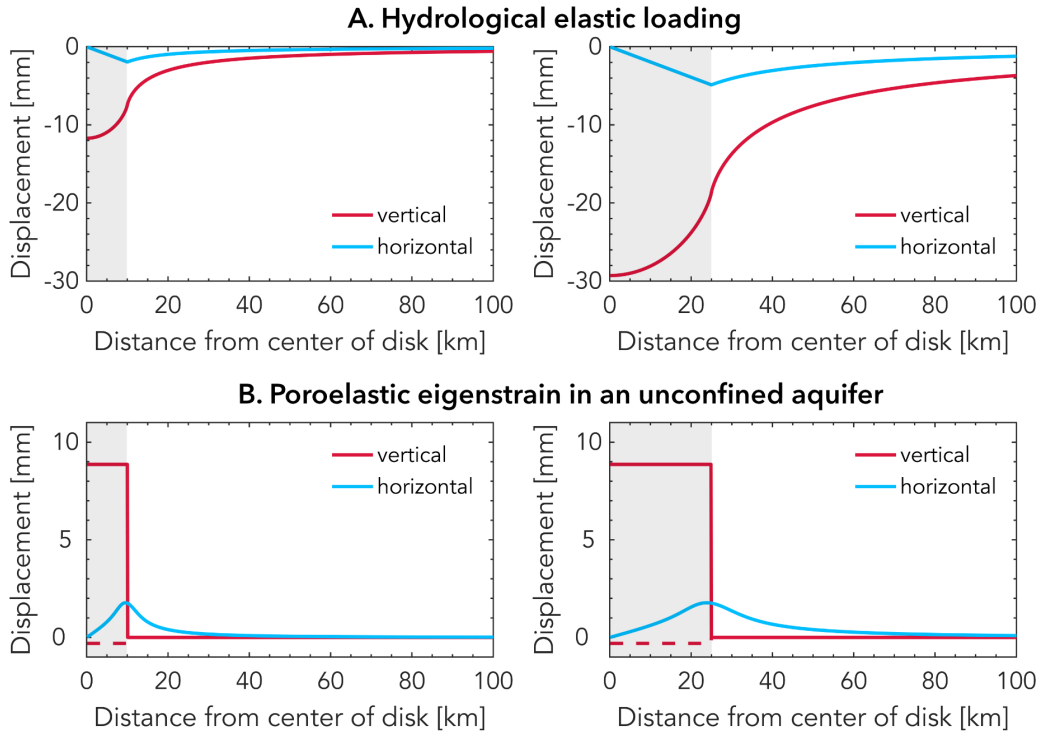


**Figure 6: Surface displacements due to hydrological elastic loading vs poroelastic eigenstrain.** Vertical and horizontal surface displacements induced by **A.** a disk load at the surface of an elastic half-space and **B.** poroelastic eigenstrain in a circular unconfined aquifer as illustrated in Figure 1 for disks of radius  $a = 10$  km (left) and  $a = 25$  km (right) as indicated by the grey-shaded areas. For the vertical poroelastic deformation, the dashed line represents the shear-induced deformation while the solid line represents the total poroelastic displacement. The increase in surface water level,  $P$ , and groundwater level,  $\Delta h$ , are set at 5 and 20 m, respectively, consistent with a 25% porosity. Other parameter values are:  $\nu = 0.25$ ,  $E_{deep} = 80$  GPa,  $E_{aq} = 10$  GPa,  $\beta = 0.8$ ,  $b = 1000$  m.

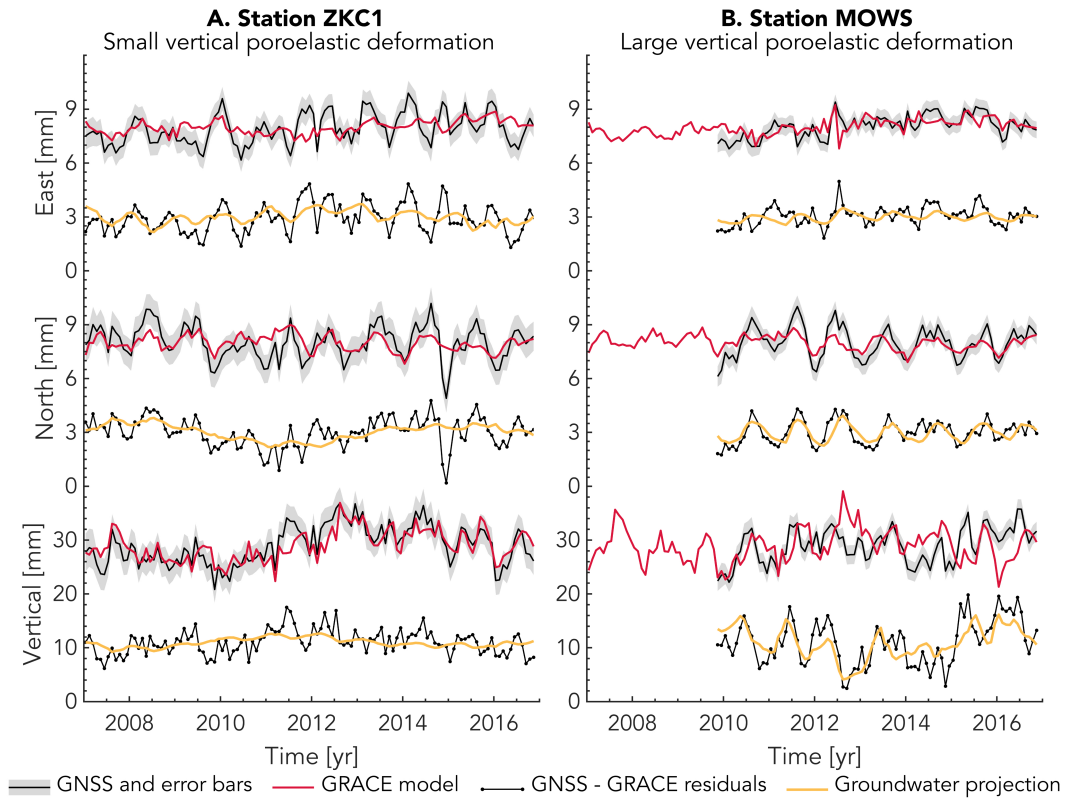


**Figure 7: Extracting the OPAS's poroelastic signal from GNSS time series.** Black lines with grey error bars are GNSS time series (corrected for degree 1). A common mode has been removed in the East and North components. Red lines are the GRACE model predictions. Black dots are the GNSS-GRACE residuals. Yellow lines are the projection of the GNSS-GRACE residuals onto the  $W_i$  from the groundwater ICA.



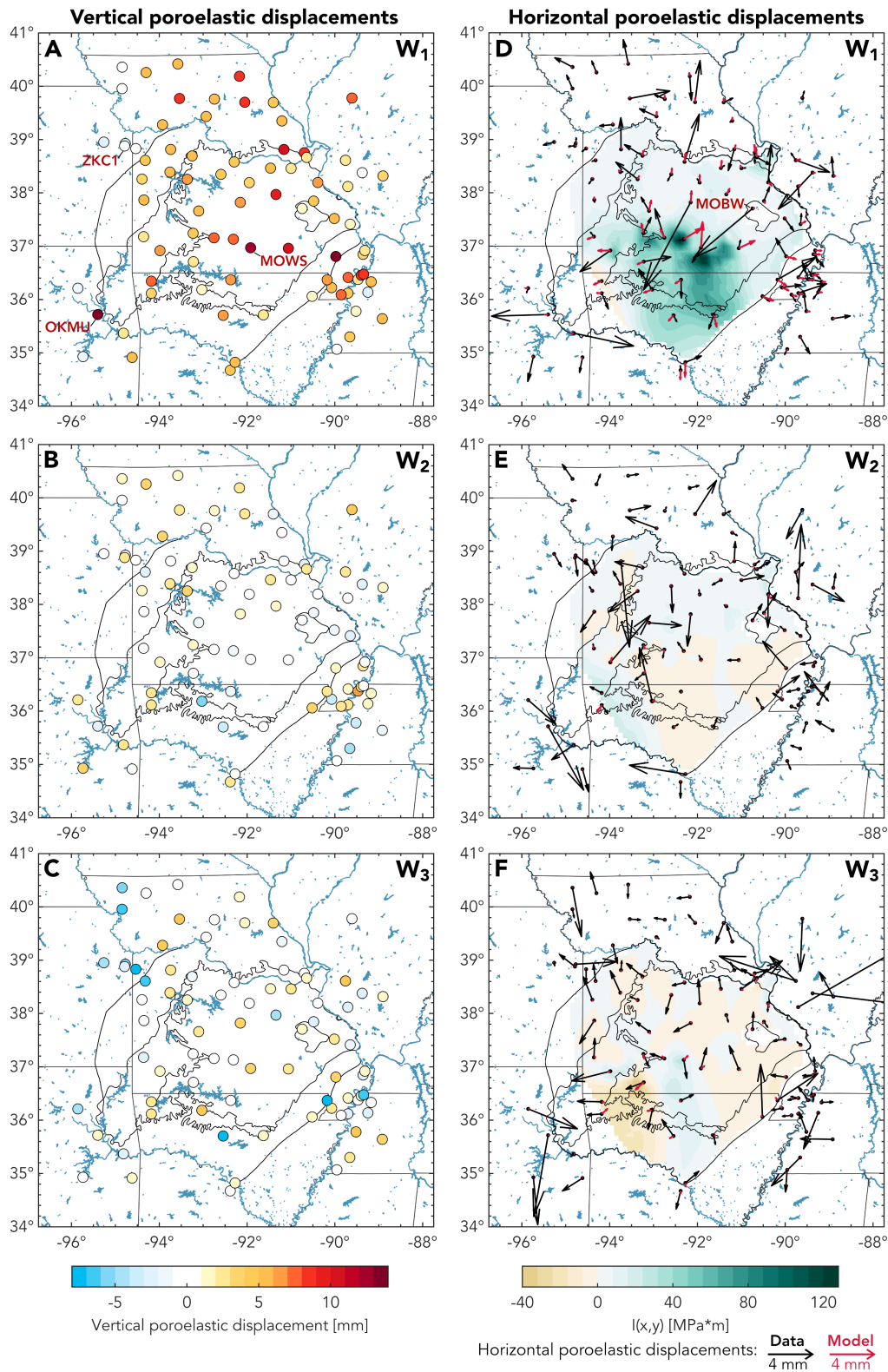


**Figure 8: Inferred poroelastic displacements and model predictions of poroelastic horizontal displacements.** Vertical (A-C) and horizontal (D-F) poroelastic displacement extracted by projecting onto the different temporal functions  $W_i$ . **D-F.** Distribution of  $I(x,y)$  from each groundwater IC and resulting horizontal poroelastic displacement (red arrows).

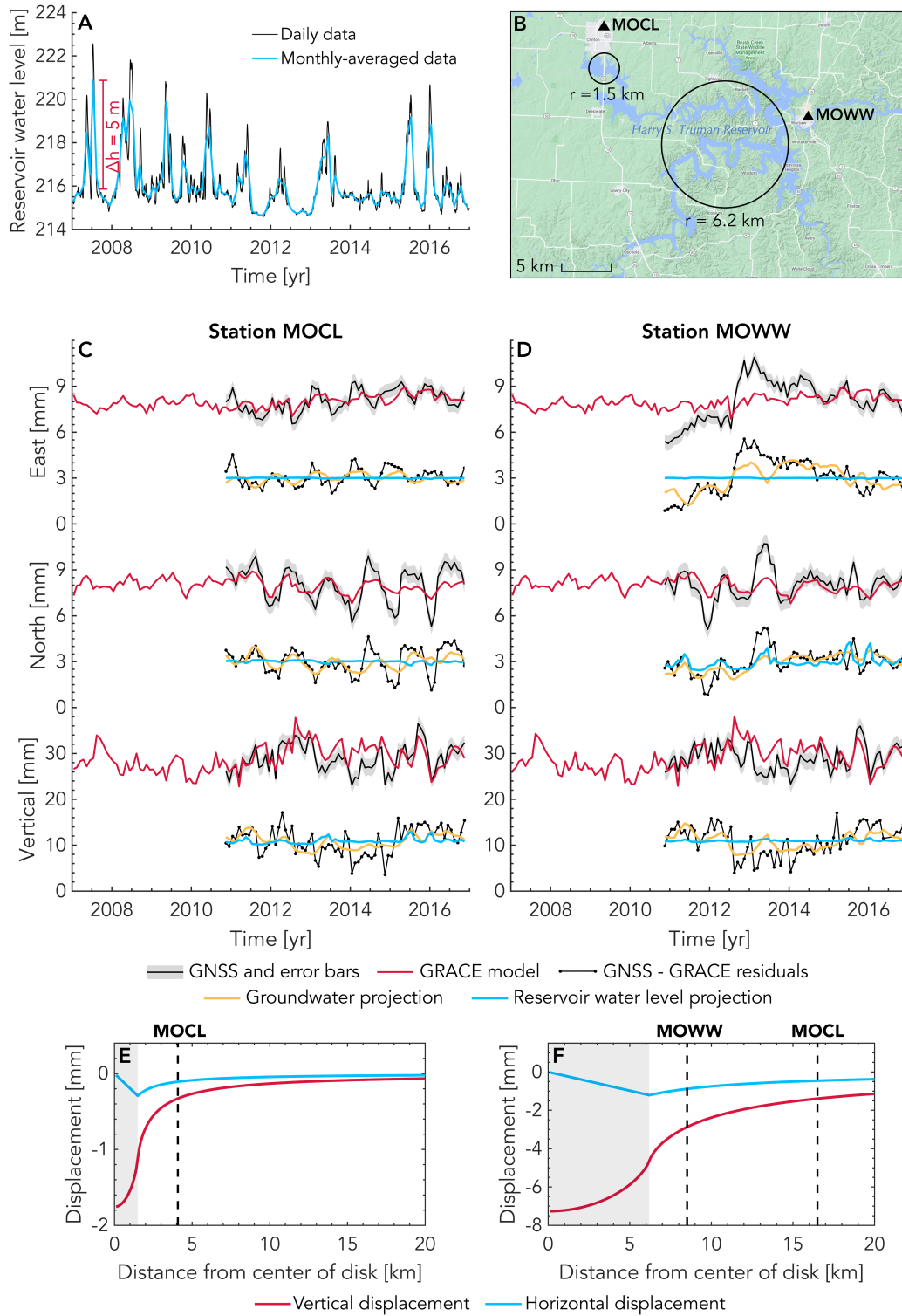


**Figure 9: Estimating the elastic loading contribution from a surface water reservoir.** (A) Daily and monthly-averaged temporal evolution of water levels at the Harry S. Truman Reservoir. (B) Location of GNSS stations MOCL and MOWW with respect to the reservoir. (C,D) Same as Figures 7 and S2 but with projections of the GNSS-GRACE residuals onto reservoir water levels (blue). (E,F) Displacements associated with the analytical elastic loading model (as in Figure 6A) for the circular regions shown in (B) and a 5m increase in water level.

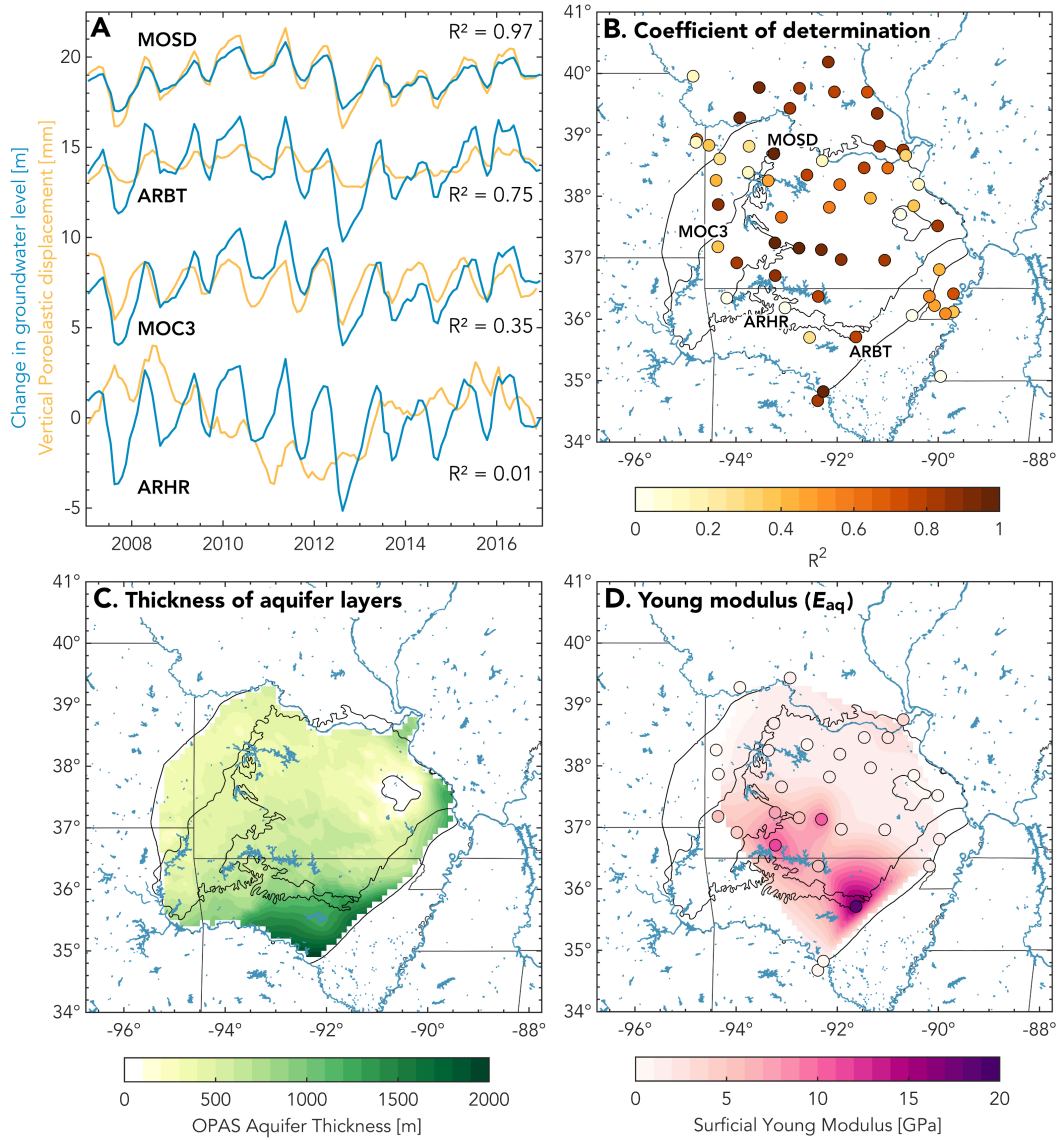


**Figure 10: Estimating aquifer Young modulus from vertical poroelastic displacement and groundwater level variations** **A.** Examples of vertical poroelastic displacement time series and groundwater level change extracted with ICA and interpolated at the GNSS stations location. Note that the time series are offsetted for illustration purposes. **B.** Coefficient of determination ( $R^2$ ) of a linear fit through poroelastic displacement vs change in groundwater level. The higher  $R^2$ , the better the  $E_{aq}$  estimate. **C.** Total thickness of the aquifer layers. **D.** Young's Modulus computed for  $R^2 > 0.35$  and where all three input variables are available.

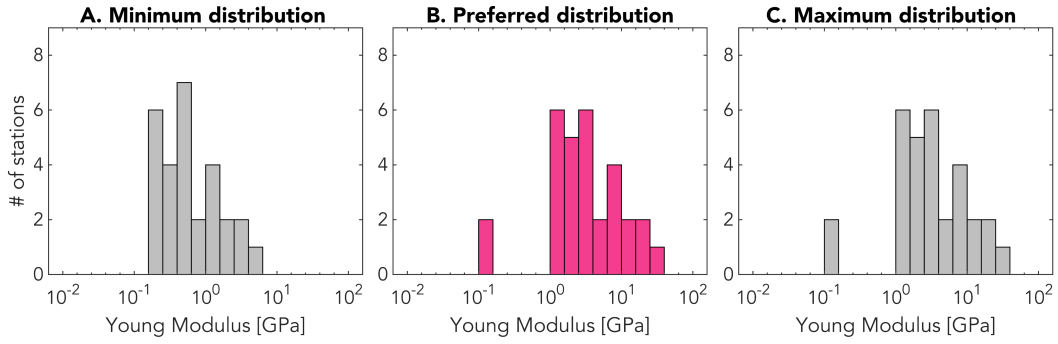


**Figure 11: Inferred distributions of aquifer Young modulus.** The preferred distribution (B) is computed with  $\nu = 0.25$ ,  $\beta = 0.80$ ,  $\phi = 0.25$ , and  $b = b_{model}$  while the minimum (A) and maximum (C) distributions are computed with  $\nu = 0.33$  and  $0.25$ ,  $\beta = 0.6$  and  $0.9$ ,  $\phi = 0.40$  and  $0.00$ , and  $b = b_{model} \mp 36$  m, respectively. Note that two stations were removed for the minimum distribution as the aquifer thickness becomes negative when subtracting 36 m.

## Appendix A Arbitrary 2D poroelastic eigenstrains in an elastic half-space

When the 2D spatial distribution is arbitrary, quantity  $I$  defined in Equation (14) can be rewritten in Cartesian coordinates as:

$$I(x, y) = \int_0^b \frac{E_{aq}(x, y)\varepsilon_{eig}(x, y) - \nu(x, y)\sigma_{zz}(x, y)}{1 - \nu(x, y)} \partial z \quad (\text{A1})$$

We can decompose  $I(x, y)$  into its Fourier components as:

$$\begin{aligned} I(x, y) = & \sum_{k_x, k_y} A_1(k_x, k_y) \cos(k_x x) \cos(k_y y) + A_2(k_x, k_y) \cos(k_x x) \sin(k_y y) \\ & + A_3(k_x, k_y) \sin(k_x x) \cos(k_y y) + A_4(k_x, k_y) \sin(k_x x) \sin(k_y y) \end{aligned} \quad (\text{A2})$$

where  $k_x$  and  $k_y$  are the wavenumbers in the  $x$  and  $y$  directions. Similar to Equation (22), the horizontal displacement field can then be computed as:

$$\begin{aligned} u_x = & \frac{2(1 - \nu^2)}{E_{deep}} \sum_{k_x, k_y} -A_1(k_x, k_y) \sin(k_x x) \cos(k_y y) - A_2(k_x, k_y) \sin(k_x x) \sin(k_y y) \\ & + A_3(k_x, k_y) \cos(k_x x) \cos(k_y y) + A_4(k_x, k_y) \cos(k_x x) \sin(k_y y) \end{aligned} \quad (\text{A3})$$

$$\begin{aligned} u_y = & \frac{2(1 - \nu^2)}{E_{deep}} \sum_{k_x, k_y} -A_1(k_x, k_y) \cos(k_x x) \sin(k_y y) + A_2(k_x, k_y) \cos(k_x x) \cos(k_y y) \\ & - A_3(k_x, k_y) \sin(k_x x) \sin(k_y y) + A_4(k_x, k_y) \sin(k_x x) \cos(k_y y) \end{aligned} \quad (\text{A4})$$

## Appendix B Analytical elastic loading solution for $r \rightarrow a$

Since  $\mathcal{K}(k)$  in Equation (22) diverges when  $r = a$ , the solution diverges at  $r = a$ . However, we can express and evaluate the  $\mathcal{K}(k)$  and  $\mathcal{E}(k)$  terms with infinite series truncated for an arbitrary  $n$  to numerically approach the solution at  $r = a$ :

$$\left(\frac{2}{k^2} - 1\right) \mathcal{K}(k) - \frac{2}{k^2} \mathcal{E}(k) = \frac{\pi}{2} \sum_{n=0}^{\infty} \frac{n}{n+1} \left(\frac{(2n)!}{2^{2n}(n!)^2}\right)^2 k^{2n} \quad (\text{B1})$$

## Acknowledgments

The USGS groundwater level, CSR GRACE and NGL GNSS time series used in this work are available at <https://waterservices.usgs.gov>, [https://podaac.jpl.nasa.gov/dataset/GRACE\\_GSM\\_L2\\_GRAV\\_CSR\\_RL06](https://podaac.jpl.nasa.gov/dataset/GRACE_GSM_L2_GRAV_CSR_RL06) and <http://geodesy.unr.edu>, respectively. The Ozark Plateaus Aquifer System model of Westerman et al. (2016) is available at <http://dx.doi.org/10.5066/F7HQ3X0T>. This study was supported by the National Sciences and Engineering Research Council of Canada through a post-graduate doctoral scholarship (PGSD-3-517078-2018), the Office for Science and Technology of the Embassy of France in the United States through a STEM Chateaubriand Fellowship as well as the Institut de Physique du Globe de Paris (IPGP contribution #4232). The authors would like to thank the editor, Paul Tregoning, and two anonymous reviewers for their constructive comments which have led to an improved manuscript as well as Roland Bruggmann for insightful discussions. SL would also like to thank Katherine Knierim for providing helpful resources to map OPAS as well as Wilbur Shirley for help with the Fourier analysis.

## References

Adusumilli, S., Borsa, A. A., Fish, M. A., McMillan, H. K., & Silverii, F. (2019). A Decade of Water Storage Changes Across the Contiguous United States From

- 769 GPS and satellite gravity. *Geophysical Research Letters*, 2019GL085370. doi:  
770 10.1029/2019GL085370
- 771 Alghamdi, A., Hesse, M. A., Chen, J., & Ghattas, O. (2020). Bayesian Poroelastic  
772 Aquifer Characterization From InSAR Surface Deformation Data. Part I: Maxi-  
773 mum A Posteriori Estimate. *Water Resources Research*, 56(10), e2020WR027391.  
774 Retrieved from <https://onlinelibrary.wiley.com/doi/10.1029/2020WR027391>  
775 doi: 10.1029/2020WR027391
- 776 Altamimi, Z., Rebischung, P., Métivier, L., & Collilieux, X. (2016). ITRF2014: A  
777 new release of the International Terrestrial Reference Frame modeling nonlinear  
778 station motions. *Journal of Geophysical Research: Solid Earth*, 121(8), 6109–6131.  
779 doi: 10.1002/2016JB013098
- 780 Amelung, F., Galloway, D. L., Bell, J. W., Zebker, H. A., & Lacznia, R. J. (1999,  
781 6). Sensing the ups and downs of las vegas: Insar reveals structural control of land  
782 subsidence and aquifer-system deformation. *Geology*, 27, 483. doi: 10.1130/0091-  
783 -7613(1999)027<0483:STUADO>2.3.CO;2
- 784 Argus, D. F., Fu, Y., & Landerer, F. W. (2014). Seasonal variation in total water  
785 storage in California inferred from GPS observations of vertical land motion. *Geo-  
786 physical Research Letters*, 41(6), 1971–1980. doi: 10.1002/2014GL059570
- 787 Argus, D. F., Landerer, F. W., Wiese, D. N., Martens, H. R., Fu, Y., Famiglietti,  
788 J. S., ... Watkins, M. M. (2017, dec). Sustained Water Loss in California's  
789 Mountain Ranges During Severe Drought From 2012 to 2015 Inferred From  
790 GPS. *Journal of Geophysical Research: Solid Earth*, 122(12), 10,559–10,585.  
791 doi: 10.1002/2017JB014424
- 792 Bailly, C., Fortin, J., Adelinet, M., & Hamon, Y. (2019, dec). Upscaling of Elastic  
793 Properties in Carbonates: A Modeling Approach Based on a Multiscale Geophys-  
794 ical Data Set. *Journal of Geophysical Research: Solid Earth*, 124(12), 13021–  
795 13038. doi: 10.1029/2019JB018391
- 796 Barbot, S., Moore, J. D., & Lambert, V. (2017). Displacement and stress associated  
797 with distributed anelastic deformation in a half-space. *Bulletin of the Seismologi-  
798 cal Society of America*, 107. doi: 10.1785/0120160237
- 799 Bayless, E. R., Arihood, L. D., Reeves, H. W., Sperl, B. J., Qi, S. L., Stipe, V. E.,  
800 & Bunch, A. R. (2017). *Maps and grids of hydrogeologic information created  
801 from standardized water-well drillers' records of the glaciated United States* (Tech.  
802 Rep.). doi: 10.3133/sir20155105
- 803 Bell, J. W., Amelung, F., Ferretti, A., Bianchi, M., & Novali, F. (2008, 2). Per-  
804 manent scatterer insar reveals seasonal and long-term aquifer-system response to  
805 groundwater pumping and artificial recharge. *Water Resources Research*, 44. doi:  
806 10.1029/2007WR006152
- 807 Bettadpur, S. (2018). Gravity Recovery and Climate Experiment Level-2 Gravity  
808 Field Product User Handbook. , 734, 1–21.
- 809 Bettinelli, P., Avouac, J.-P., Flouzat, M., Bollinger, L., Ramillien, G., Rajaure, S.,  
810 & Sapkota, S. (2008). Seasonal variations of seismicity and geodetic strain in the  
811 Himalaya induced by surface hydrology. *Earth and Planetary Science Letters*,  
812 266(3-4), 332–344. doi: 10.1016/J.EPSL.2007.11.021
- 813 Bevis, M., & Brown, A. (2014). Trajectory models and reference frames for crustal  
814 motion geodesy. *Journal of Geodesy*, 88(3), 283–311. doi: 10.1007/s00190-013-  
815 -0685-5
- 816 Blewitt, G., Hammond, W. C., & Kreemer, C. (2018). Harnessing the GPS data ex-  
817 plosion for interdisciplinary science. *Eos*, 99. doi: 10.1029/2018EO104623
- 818 Blewitt, G., Lavallée, D., Clarke, P., & Nurutdinov, K. (2001). A new global  
819 mode of Earth deformation: seasonal cycle detected. *Science (New York, N. Y.)*,  
820 294(5550), 2342–5. doi: 10.1126/science.1065328
- 821 Borsa, A. A., Agnew, D. C., & Cayan, D. R. (2014, sep). Ongoing drought-induced  
822 uplift in the western United States. *Science*, 345(6204), 1587–1590. doi: 10.1126/

823  
824  
825  
826  
827  
828  
829  
830  
831  
832  
833  
834  
835  
836  
837  
838  
839  
840  
841  
842  
843  
844  
845  
846  
847  
848  
849  
850  
851  
852  
853  
854  
855  
856  
857  
858  
859  
860  
861  
862  
863  
864  
865  
866  
867  
868  
869  
870  
871  
872  
873  
874  
875  
876

SCIENCE.1260279

- Boussinesq, J. (1885). *Application des potentiels l'étude de l'équilibre et du mouvement des solides lastiques*. Blanchard: Reprint Paris.
- Calais, E., Camelbeeck, T., Stein, S., Liu, M., & Craig, T. J. (2016). A new paradigm for large earthquakes in stable continental plate interiors. *Geophysical Research Letters*, *43*(20), 10,621–10,637. doi: 10.1002/2016GL070815
- Carlson, G., Shirzaei, M., Ojha, C., & Werth, S. (2020, 9). Subsidence-derived volumetric strain models for mapping extensional fissures and constraining rock mechanical properties in the San Joaquin Valley, California. *Journal of Geophysical Research: Solid Earth*, *125*. Retrieved from <https://onlinelibrary.wiley.com/doi/10.1029/2020JB019980> doi: 10.1029/2020JB019980
- Chanard, K., Fleitout, L., Calais, E., Rebischung, P., & Avouac, J. (2018). Toward a Global Horizontal and Vertical Elastic Load Deformation Model Derived from GRACE and GNSS Station Position Time Series. *Journal of Geophysical Research: Solid Earth*, *123*(4), 3225–3237. doi: 10.1002/2017JB015245
- Chanard, K., Métois, M., Rebischung, P., & Avouac, J.-P. (2020). A warning against over-interpretation of seasonal signals measured by the Global Navigation Satellite System. *Nature Communications*, *11*(1), 1375. doi: 10.1038/s41467-020-15100-7
- Chaussard, E., Bürgmann, R., Shirzaei, M., Fielding, E. J., & Baker, B. (2014). Predictability of hydraulic head changes and characterization of aquifer-system and fault properties from InSAR-derived ground deformation. *Journal of Geophysical Research: Solid Earth*, *119*(8), 6572–6590. doi: 10.1002/2014JB011266
- Chaussard, E., Milillo, P., Bürgmann, R., Perissin, D., Fielding, E. J., & Baker, B. (2017). Remote Sensing of Ground Deformation for Monitoring Groundwater Management Practices: Application to the Santa Clara Valley During the 2012–2015 California Drought. *Journal of Geophysical Research: Solid Earth*, *122*(10), 8566–8582. doi: 10.1002/2017JB014676
- Choudrey, R. (2002). Variational methods for Bayesian independent component analysis. *Robots.Ox.Ac.Uk*, 261. Retrieved from <http://www.robots.ox.ac.uk/~parg/projects/ica/riz/Pubs/thesis.ps.gz>
- Craig, T. J., & Calais, E. (2014). Strain accumulation in the New Madrid and Wabash Valley seismic zones from 14 years of continuous GPS observation. *Journal of Geophysical Research: Solid Earth*, *119*(12), 9110–9129.
- Craig, T. J., Chanard, K., & Calais, E. (2017). Hydrologically-driven crustal stresses and seismicity in the New Madrid Seismic Zone. *Nature Communications*, *8*(1), 2143. doi: 10.1038/s41467-017-01696-w
- Domenico, P. A. P. A., & Schwartz, F. W. F. W. (1998). *Physical and chemical hydrogeology*. Wiley.
- Dong, D., Fang, P., Bock, Y., Cheng, M. K., & Miyazaki, S. (2002). Anatomy of apparent seasonal variations from GPS-derived site position time series. *Journal of Geophysical Research: Solid Earth*, *107*(B4), ETG 9–1–ETG 9–16. doi: 10.1029/2001JB000573
- Farrell, W. E. (1972). Deformation of the Earth by surface loads. *Reviews of Geophysics*, *10*(3), 761. doi: 10.1029/RG010i003p00761
- Ferreira, V., Ndehedehe, C., Montecino, H., Yong, B., Yuan, P., Abdalla, A., & Mohammed, A. (2019). Prospects for Imaging Terrestrial Water Storage in South America Using Daily GPS Observations. *Remote Sensing*, *11*(6), 679. doi: 10.3390/rs11060679
- Ferronato, M., Castelletto, N., & Gambolati, G. (2010). A fully coupled 3-d mixed finite element model of biot consolidation. *Journal of Computational Physics*, *229*. doi: 10.1016/j.jcp.2010.03.018
- Fleitout, L., & Chanard, K. (2018, December). Displacements and Stresses Induced by Temperature and Poroelastic Pressure Variations in the Surficial Layers for an Earth with Realistic Elastic Properties. In *Agu fall meeting abstracts* (Vol. 2018,

- 877 p. G53B-03).
- 878 Fortin, J., Guéguen, Y., & Schubnel, A. (2007, aug). Effects of pore collapse and  
879 grain crushing on ultrasonic velocities and  $V_p/V_s$ . *Journal of Geophysical Re-*  
880 *search: Solid Earth*, 112(8). doi: 10.1029/2005JB004005
- 881 Fu, Y., Argus, D. F., & Landerer, F. W. (2015). GPS as an independent mea-  
882 surement to estimate terrestrial water storage variations in Washington and  
883 Oregon. *Journal of Geophysical Research: Solid Earth*, 120(1), 552–566. doi:  
884 10.1002/2014JB011415
- 885 Galloway, D. L., & Burbey, T. J. (2011). Review: Regional land subsidence accom-  
886 panying groundwater extraction. *Hydrogeology Journal*, 19(8), 1459–1486. doi: 10  
887 .1007/s10040-011-0775-5
- 888 Ge, S., & Garven, G. (1992). Hydromechanical modeling of tectonically driven  
889 groundwater flow with application to the Arkoma Foreland Basin. *Journal of Geo-*  
890 *physical Research*, 97(B6), 9119. doi: 10.1029/92JB00677
- 891 Gleeson, T., Wagener, T., Döll, P., Zipper, S. C., West, C., Wada, Y., ... Bierkens,  
892 M. F. P. (2021). Gmd perspective: the quest to improve the evaluation of  
893 groundwater representation in continental to global scale models. *Geoscientific*  
894 *Model Development Discussions*, 2021, 1–59. Retrieved from [https://](https://gmd.copernicus.org/preprints/gmd-2021-97/)  
895 [gmd.copernicus.org/preprints/gmd-2021-97/](https://gmd.copernicus.org/preprints/gmd-2021-97/) doi: 10.5194/gmd-2021-97
- 896 GRACE. (2018). GRACE FIELD GEOPOTENTIAL COEFFICIENTS CSR RE-  
897 LEASE 6.0 Ver. 6.0 PO.DAAC, CA, USA.  
898 doi: 10.5067/GRGSM-20C06
- 899 Gualandi, A., & Liu, Z. (2021). Variational bayesian independent component  
900 analysis for insar displacement timeseries with application to central california,  
901 usa. *Journal of Geophysical Research: Solid Earth*, 126, e2020JB020845. doi:  
902 10.1029/2020JB020845
- 903 Gualandi, A., Serpelloni, E., & Belardinelli, M. E. (2016). Blind source separation  
904 problem in GPS time series. *Journal of Geodesy*, 90(4), 323–341. doi: 10.1007/  
905 s00190-015-0875-4
- 906 Hart, R. M., Clark, B. R., & Bolyard, S. E. (2008). *Digital Surfaces and Thick-*  
907 *nesses of Selected Hydrogeologic Units within the Mississippi Embayment Regional*  
908 *Aquifer Study (MERAS)* (Tech. Rep.).
- 909 Hays, P. D., Knierim, K. J., Breaker, B., Westerman, D. A., & Clark, B. R. (2016).  
910 Hydrogeology and hydrologic conditions of the Ozark Plateaus aquifer system.  
911 *U.S. Geological Survey Scientific Investigations Report*(2016-5137), 61.
- 912 Helm, D. C. (1994). Horizontal aquifer movement in a theisthiem confined system.  
913 *Water Resources Research*, 30. doi: 10.1029/94WR00030
- 914 Hoffmann, L. S. G. D. L., J., & Wilson, A. (2003). *Modflow-2000 ground-water*  
915 *modeluser guide to the subsidence and aquifer-system compaction (sub) package*  
916 (Tech. Rep.).
- 917 Hu, X., & Bürgmann, R. (2020). Aquifer deformation and active faulting in Salt  
918 Lake Valley, Utah, USA. *Earth and Planetary Science Letters*, 547, 116471. doi:  
919 10.1016/J.EPSL.2020.116471
- 920 Imes, J. L. (1989). Analysis of the effect of pumping on groundwater flow in the  
921 Springfield Plateau and Ozark Aquifers near Springfield, Missouri. *Water Re-*  
922 *sources Investigations Report*, 89-4079.
- 923 Imes, J. L., & Emmett, L. F. (1994). Geohydrology of the Ozark Plateaus aquifer  
924 system in parts of Missouri, Arkansas, Oklahoma, and Kansas. *US Geological Sur-*  
925 *vey Professional Paper*, 1414 D. doi: 10.3133/pp1414d
- 926 Johnson. (1987). *Contact mechanics*. Cambridge University Press.
- 927 Johnson, C. W., Fu, Y., & Bürgmann, R. (2017). Seasonal water storage, stress  
928 modulation, and California seismicity. *Science (New York, N.Y.)*, 356(6343),  
929 1161–1164. doi: 10.1126/science.aak9547



- 930 King, N. E., Argus, D., Langbein, J., Agnew, D. C., Bawden, G., Dollar, R. S., . . .  
 931 Barseghian, D. (2007). Space geodetic observation of expansion of the San Gabriel  
 932 Valley, California, aquifer system, during heavy rainfall in winter 20042005. *Jour-*  
 933 *nal of Geophysical Research*, *112*(B3), B03409. doi: 10.1029/2006JB004448
- 934 Knierim, K. J., Nottmeier, A. M., Worland, S., Westerman, D. A., & Clark, B. R.  
 935 (2017). Challenges for creating a site-specific groundwater-use record for the  
 936 Ozark Plateaus aquifer system (central USA) from 1900 to 2010. *Hydrogeology*  
 937 *Journal*. doi: 10.1007/s10040-017-1593-1
- 938 Kusche, J., Schmidt, R., Petrovic, S., & Rietbroek, R. (2009). Decorrelated grace  
 939 time-variable gravity solutions by gfz, and their validation using a hydrological  
 940 model. *Journal of geodesy*, *83*(10), 903–913.
- 941 Larochelle, S., Gualandi, A., Chanard, K., & Avouac, J. P. (2018). Identifica-  
 942 tion and Extraction of Seasonal Geodetic Signals Due to Surface Load Varia-  
 943 tions. *Journal of Geophysical Research: Solid Earth*, *123*(12), 11,031–11,047. doi:  
 944 10.1029/2018JB016607
- 945 Li, W., van Dam, T., Li, Z., & Shen, Y. (2016). Annual variation detected by gps,  
 946 grace and loading models. *Studia Geophysica et Geodaetica*, *60*(4), 608–621.
- 947 Longuevergne, L., Florsch, N., & Elsass, P. (2007, 4). Extracting coherent regional  
 948 information from local measurements with karhunen-love transform: Case study  
 949 of an alluvial aquifer (rhine valley, france and germany). *Water Resources Re-*  
 950 *search*, *43*. Retrieved from <http://doi.wiley.com/10.1029/2006WR005000> doi:  
 951 10.1029/2006WR005000
- 952 MATLAB. (2017). *9.3.0.713579 (r2017b)*. Natick, Massachusetts: The MathWorks  
 953 Inc.
- 954 Matonti, C., Guglielmi, Y., Viseur, S., Bruna, P., Borgomano, J., Dahl, C., & Marié,  
 955 L. (2015, jan). Heterogeneities and diagenetic control on the spatial distribution  
 956 of carbonate rocks acoustic properties at the outcrop scale. *Tectonophysics*, *638*,  
 957 94–111. Retrieved from <https://www.sciencedirect.com/science/article/pii/S0040195114005666> doi: 10.1016/J.TECTO.2014.10.020
- 958 Michel, S., Gualandi, A., & Avouac, J.-P. (2019). Interseismic coupling and slow slip  
 959 events on the cascadia megathrust. *Pure and Applied Geophysics*, *176*(9), 3867–  
 960 3891.
- 961 Miller, M. M., Shirzaei, M., & Argus, D. (2017). Aquifer Mechanical Properties and  
 962 Decelerated Compaction in Tucson, Arizona. *Journal of Geophysical Research:*  
 963 *Solid Earth*, *122*(10), 8402–8416. doi: 10.1002/2017JB014531
- 964 Mura, T. (1982). *General theory of eigenstrains*. Springer Netherlands. doi: 10.1007/  
 965 978-94-011-9306-1\_1
- 966 Ojha, C., Shirzaei, M., Werth, S., Argus, D. F., & Farr, T. G. (2018). Sus-  
 967 tained Groundwater Loss in California’s Central Valley Exacerbated by In-  
 968 tense Drought Periods. *Water Resources Research*, *54*(7), 4449–4460. doi:  
 969 10.1029/2017WR022250
- 970 Ouellette, K. J., de Linage, C., & Famiglietti, J. S. (2013). Estimating snow wa-  
 971 ter equivalent from GPS vertical site-position observations in the western United  
 972 States. *Water Resources Research*, *49*(5), 2508–2518. doi: 10.1002/wrcr.20173
- 973 Riel, B., Simons, M., Ponti, D., Agram, P., & Jolivet, R. (2018). Quantifying  
 974 Ground Deformation in the Los Angeles and Santa Ana Coastal Basins Due to  
 975 Groundwater Withdrawal. *Water Resources Research*, *54*(5), 3557–3582. doi:  
 976 10.1029/2017WR021978
- 977 Roberts, S., & Everson, R. (Eds.). (2001). *Independent Component Analysis*. Cam-  
 978 bridge University Press. doi: 10.1017/CBO9780511624148
- 979 Serpelloni, E., Pintori, F., Gualandi, A., Scocimarro, E., Cavaliere, A., Ander-  
 980 lini, L., . . . Todesco, M. (2018). Hydrologically Induced Karst Deforma-  
 981 tion: Insights From GPS Measurements in the AdriaEurasia Plate Boundary  
 982 Zone. *Journal of Geophysical Research: Solid Earth*, *123*(5), 4413–4430. doi:  
 983

- 984 10.1002/2017JB015252  
985 Shiklomanov, I. (1993). World fresh water resources. In P. H. Gleick (Ed.), *Water in*  
986 *crisis: A guide to the world's fresh water resources*. Oxford University Press.
- 987 Silverii, F., D'Agostino, N., Borsa, A. A., Calcaterra, S., Gambino, P., Giuliani, R.,  
988 & Mattone, M. (2019, jan). Transient crustal deformation from karst aquifers  
989 hydrology in the Apennines (Italy). *Earth and Planetary Science Letters*, *506*,  
990 23–37. doi: 10.1016/J.EPSL.2018.10.019
- 991 Silverii, F., D'Agostino, N., Mtois, M., Fiorillo, F., & Ventafridda, G. (2016, nov).  
992 Transient deformation of karst aquifers due to seasonal and multiyear groundwater  
993 variations observed by GPS in southern Apennines (Italy). *Journal of Geophysical*  
994 *Research: Solid Earth*, *121*(11), 8315–8337. doi: 10.1002/2016JB013361
- 995 Tapley, B. D., Bettadpur, S., Ries, J. C., Thompson, P. F., & Watkins, M. M.  
996 (2004). Grace measurements of mass variability in the earth system. *Science*,  
997 *305*(5683), 503–505.
- 998 Tsai, V. C. (2011, apr). A model for seasonal changes in GPS positions and seismic  
999 wave speeds due to thermoelastic and hydrologic variations. *Journal of Geophys-*  
1000 *ical Research*, *116*(B4), B04404. doi: 10.1029/2010JB008156
- 1001 van Dam, T., Wahr, J., Milly, P. C. D., Shmakin, A. B., Blewitt, G., Lavallée, D.,  
1002 & Larson, K. M. (2001). Crustal displacements due to continental water loading.  
1003 *Geophysical Research Letters*, *28*(4), 651–654. doi: 10.1029/2000GL012120
- 1004 Vergnolle, M., Walpersdorf, A., Kostoglodov, V., Tregoning, P., Santiago, J., Cotte,  
1005 N., & Franco, S. (2010). Slow slip events in mexico revised from the processing of  
1006 11 year gps observations. *Journal of Geophysical Research: Solid Earth*, *115*(B8).
- 1007 Verruijt, A. (2009). Elastostatics of a Half Space. In *An introduction to soil dynam-*  
1008 *ics*. doi: 10.1007/978-90-481-3441-0
- 1009 Walsh, J. B. (1965). The effect of cracks on the compressibility of rock. *Journal of*  
1010 *Geophysical Research (1896-1977)*, *70*(2), 381–389. doi: [https://doi.org/10.1029/](https://doi.org/10.1029/JZ070i002p00381)  
1011 [JZ070i002p00381](https://doi.org/10.1029/JZ070i002p00381)
- 1012 Wang, H. F. (2000). *Theory of Linear Poroelasticity with Applications to Geome-*  
1013 *chanics and Hydrogeology*. Princeton University Press.
- 1014 Westerman, D. A., Gillip, J. A., Richards, J. M., Hays, P. D., & Clark, B. R. (2016).  
1015 Altitudes and thicknesses of hydrogeologic units of the ozark plateaus aquifer sys-  
1016 tem in arkansas, kansas, missouri, and oklahoma. *U.S. Geological Survey Scientific*  
1017 *Investigations Report*(2016-5130), 32.
- 1018 Wisely, B. A., & Schmidt, D. (2010, 3). Deciphering vertical deformation and  
1019 poroelastic parameters in a tectonically active fault-bound aquifer using insar  
1020 and well level data, san bernardino basin, california. *Geophysical Journal In-*  
1021 *ternational*, *181*, 1185–1200. Retrieved from [https://academic.oup.com/](https://academic.oup.com/gji/article-lookup/doi/10.1111/j.1365-246X.2010.04568.x)  
1022 [gji/article-lookup/doi/10.1111/j.1365-246X.2010.04568.x](https://academic.oup.com/gji/article-lookup/doi/10.1111/j.1365-246X.2010.04568.x) doi:  
1023 [10.1111/j.1365-246X.2010.04568.x](https://doi.org/10.1111/j.1365-246X.2010.04568.x)